Combustion Theory and Modelling
Publication details, including instructions for authors and subscription information:
http://www.tandfonline.com/loi/tctm20

Modelling effects of subgrid-scale mixture fraction variance in LES of a piloted diffusion flame

Konstantin A. Kemenov [a], Haifeng Wang [a] & Stephen B. Pope [a]
[a] Sibley School of Mechanical and Aerospace Engineering, Cornell University, Ithaca, NY, 14853, USA

Version of record first published: 09 Jan 2012

To cite this article: Konstantin A. Kemenov, Haifeng Wang & Stephen B. Pope (2012): Modelling effects of subgrid-scale mixture fraction variance in LES of a piloted diffusion flame, Combustion Theory and Modelling, 16:4, 611-638

To link to this article: http://dx.doi.org/10.1080/13647830.2011.645881

Combustion Theory and Modelling
Vol. 16, No. 4, 2012, 611–638

Taylor & Francis
Taylor & Francis Group

Modelling effects of subgrid-scale mixture fraction variance in LES of a piloted diffusion flame

Konstantin A. Kemenov*, Haifeng Wang and Stephen B. Pope

Sibley School of Mechanical and Aerospace Engineering, Cornell University, Ithaca, NY 14853, USA

(*Received 30 September 2010; final version received 13 November 2011*)

A posteriori analysis of the statistics of two large-eddy simulation (LES) solutions describing a piloted methane–air (Sandia D) flame is performed on a series of grids with progressively increased resolution reaching about 10.5 million cells. Chemical compositions, density and temperature fields are modelled with a steady flamelet approach and parametrised by the mixture fraction. The difference between the LES solutions arises from a different numerical treatment of the subgrid scale (SGS) mixture fraction variance – an important quantity of interest in non-premixed combustion modelling. In the first case (model I), the variance transport equation is solved directly, while in the second (model II), an equation for the square of the mixture fraction is solved, and the variance is computed from its definition. The comparison of the LES solutions is based on the convergence properties of their statistics with respect to the turbulence resolution length scale. The dependence of the LES statistics is analysed for velocity and the mixture fraction fields, and tested for convergence. For the most part, the statistics converge for the finest grids, but the variance of the mixture fraction shows some residual grid dependence in the high-gradient regions of the jet near field. The SGS variance given by model I exhibits realisability everywhere, whereas in regions of the flame model II is non-realisable, predicting negative variances. Furthermore, the LES statistics of model I exhibit superior convergence behaviour.

Keywords: subgrid-scale variance; mixture fraction; large-eddy simulation; Sandia flame D; non-premixed turbulent combustion

1. Introduction

Large-eddy simulation (LES) has proved to be an effective simulation approach for a wide range of turbulent flows including chemically reactive turbulent flows [1,2]. This latter class of flows adds an extra set of challenges to LES modelling. In addition to accounting for the effects of the unresolved dynamic scales, the small-scale molecular mixing and chemical reaction processes, which usually occur on scales much smaller than the LES grid, have to be modelled as well. A number of successful applications of LES have demonstrated the attractiveness of the approach not only for canonical geometries like laboratory jet flames but also for complex ones like gas-turbine combustors [3–6].

LES focuses on the explicit simulation of the large (resolved) scales of the turbulent motion where the effects of the unresolved scales are represented by a model. The resolved

*Corresponding author. Email: kak262@cornell.edu

ISSN: 1364-7830 print / 1741-3559 online

http://dx.doi.org/10.1080/13647830.2011.645881
http://www.tandfonline.com

LES field, say for example for the mixture fraction, $\tilde{\xi}(\boldsymbol{x}, t)$, is very often associated with spatial filtering of the underlying turbulent field $\xi(\boldsymbol{x}, t)$. While such a definition of the resolved fields can be helpful in the derivation of the LES equations, albeit under very restrictive conditions of the uniformity of filter width and commutativity between filtering and differentiation, generally it appears to be somewhat misleading since the LES field of interest is always a solution of the LES equations [7]. Furthermore, invoking the concept of filtering in deriving LES equations is at least debatable since these equations arise naturally in multiscale formulations [8] or in regularisation of the Navier–Stokes equations [9] without making use of filters. In addition, as a solution of the LES equations, the LES field depends on an artificial parameter $\Delta(\boldsymbol{x})$ – the filter width or, more appropriately, the turbulence resolution length scale [7].

In practical LES, the turbulence resolution scale $\Delta(\boldsymbol{x})$ is often taken to be equal to (or a multiple of) the characteristic length scale of an LES cell which, in turn, can be prescribed in a non-unique way. Furthermore, the turbulence resolution scale $\Delta(\boldsymbol{x})$ usually enters various models for the unclosed subgrid scale (SGS) terms which implies that the LES solutions become dependent on $\Delta(\boldsymbol{x})$. Because of the inherent randomness the predictive capabilities of LES are judged based on comparison of the LES derived statistics Q^m to the 'true' statistics Q obtained from the high-resolution experiments or, for low Re-number flows, from DNS. Generally, the LES derived statistics will depend on the SGS models as well as on the specification of $\Delta(\boldsymbol{x})$. For example, these statistics can be mean values of the resolved and full mixture fractions, i.e. $Q^m = \langle\tilde{\xi}(\boldsymbol{x}, t)\rangle$ and $Q = \langle\xi(\boldsymbol{x}, t)\rangle$ derived from an LES solution and from the full turbulent field, respectively. The objective of an LES is then to produce an accurate estimate $Q^m(\Delta) = Q^W(\Delta) + Q^r(\Delta)$ for the true statistics Q, i.e. $Q^m(\Delta) \approx Q$. Here, $Q^W(\Delta)$ and $Q^r(\Delta)$ denote the contributions to the modelled statistics from the resolved and subgrid fields, respectively. As the turbulence resolution scale goes to the DNS limit ($\Delta \to 0$) the LES solution tends to the DNS solution as the contribution from the subgrid terms vanishes. For a consistent LES model its total LES statistics $Q^m(\Delta)$ are supposed to converge to the true DNS statistics Q while the residual parts $Q^r(\Delta)$ tend to zero. As pointed out by Pope [7], different LES models can then be compared in terms of overall accuracy and cost based on the convergence of their statistics, i.e. how fast and how well the total LES statistics $Q^m(\Delta)$ approximate the true DNS statistics Q with respect to Δ. Consequently, a comparison that is based on a single value of Δ, i.e. a single LES realisation, cannot be deemed satisfactory.

The sensitivity of LES statistics to Δ gains more importance for the LES of combustion systems. In turbulent combustion, the rate-controlling processes such as reactant mixing and chemical reactions occur on small scales that are usually much smaller than Δ. As a result, the resolved effect of the complex small-scale turbulence/chemistry interactions is modelled in an affordable way by a combustion model. A question of how a particular combustion model affects LES statistics with respect to the true statistics Q can be studied based on the Δ-dependence of the total LES statistics Q^m. Studies of the turbulence resolution effects on a reactive LES solution are still quite rare in literature [6]. The present work, therefore, attempts to fill this gap partially by examining the performance of two LES models based on the convergence of their statistics with respect to Δ for the case of a non-premixed jet flame.

Many combustion models centre on a mixture fraction based flamelet approach [10], where chemical composition, temperature and density are parametrised by one (or a few) field variables such as the mixture fraction and its scalar dissipation rate, or a specially constructed progress variable [11]. While such a simplified turbulence/chemistry

interaction treatment might fall short of representing realistic combustion chemistry, as opposed to more advanced and technically elaborated approaches such as transported PDF based methods [12], it provides a useful tool to study particular effects of the SGS or/and combustion models on the LES solution. Even though the mixture fraction transport equation does not contain a source term, its solution still only approximates the resolved mixture fraction field, which necessitates accounting for the unresolved small-scale mixture fraction fluctuations on the resolved thermochemical quantities in the flamelet parametrisation. The SGS mixture fraction variance $V_\xi \equiv \widetilde{\xi^2} - \tilde{\xi}^2$ provides such a measure [13]. Usually, it enters as a parameter of the presumed probability density function such as the beta-PDF [13, 14] in the statistical representation of the resolved field, or it can be accounted for directly in a quadratically-approximated flamelet parametrisation [15]. In either case, the SGS variance requires modelling. The other attractive feature of using the SGS mixture fraction variance in simulations is that its mean value provides a simple model for the residual statistic $Q^r(\Delta)$ when the statistic of interest Q is the variance.

A number of the SGS variance models have been proposed and evaluated in the past [13, 16, 17], and recently [18–20] in the context of a priori and a posteriori LES studies of non-premixed combustion. In the present work, we consider one class of models which is based on integration of an evolution equation, either for the SGS mixture fraction variance itself (model I) [17], or for the resolved square of the mixture fraction $\widetilde{\xi^2}$ (model II) [21]. In the latter case, the SGS variance is computed from $\tilde{\xi}$, $\widetilde{\xi^2}$ and its definition $V_\xi \equiv \widetilde{\xi^2} - \tilde{\xi}^2$. Even though the inclusion of an extra evolution equation into the LES system adds to the computational expense, at the same time it avoids some strong assumptions about the resolved mixture fraction field, which are routinely invoked in more simple algebraic models, like the scale-similarity assumption based model [13], or the equilibrium model which assumes an equilibrium between production and dissipation rates [16]. An evolution equation for $\widetilde{\xi^2}$ is simpler than that for V_ξ since it does not contain the production term and is often viewed as the better choice for SGS variance modelling [18, 20]. Both models have been used in the past, in several LES-based studies of non-premixed flames. For example, Ihme and Pitsch [22] employed the variance transport equation (model I) to study extinction and reignition events in piloted methane–air flames (Sandia flames D and E) using the extended flamelet/progress variable (FPV) approach, while Raman *et al.* [21] adopted the mixture fraction square transport equation (model II) to simulate the methane–hydrogen bluff-body stabilised flame in the context of the transported filtered-density-function (FDF) method. Model II was also chosen by Triantafyllidis *et al.* [23] in an LES study of forced ignition of a bluff-body methane–air flame using the conditional moment closure (CMC) method. As both models appear to be equivalent at the continuous level, the rational choice of which one is better is not straightforward and depends on incurred numerical errors. Based on a priori analysis of the DNS data, Kaul *et al.* [20] showed that employing the variance transport equation tends to underpredict the SGS variance due to numerical errors associated with the chain-rule approximation. It is remarked here that, while a priori analysis based on the explicit filtering of the DNS data might provide some useful insights, it falls short of fully evaluating the model performance since the resolved LES fields are the solutions of the LES evolution equations and do not coincide with the filtered DNS fields [7].

Therefore, an objective of the present paper is to compare the performance of two transport equation based models for the SGS scalar variance with respect to convergence of their LES statistics on different grids for a realistic flame – Sandia flame D. This piloted non-premixed methane–air flame has been studied experimentally by Barlow and

Frank [24] and by Schneider *et al.* [25], which makes it a popular choice for testing LES models in studies of non-premixed turbulent combustion [22,26–31]. Another rationale for choosing the Sandia flame D configuration is the virtual non-existence (or absence) of re-ignition/extinction or auto-ignition events that are challenging to predict accurately in LES but which, on the other hand, allows much simpler chemistry models to be used and less sensitivity to numerical errors in the SGS variance prediction to be expected. For example, in their recent LES study of the Cabra flame, a lifted methane–air jet flame in a vitiated co-flow experimentally studied by Cabra *et al.* [32], Domingo *et al.* [33] demonstrate that the LES solution exhibits a great deal of sensitivity to the modelling of the SGS scalar dissipation rate which is usually modelled proportionally to the SGS variance and appears as a source term in the SGS variance evolution equations (see Section 2.2). In this lifted flame, autoignition, which was identified to be a primary mechanism for flame stabilisation [34], is more likely to occur in regions with low levels of the scalar dissipation rate. As a result, numerical errors associated with computation of the SGS variance could strongly affect the location of the stabilisation point and the lift-off height of the flame producing potentially different LES solutions depending on which model, I or II, is employed to compute the SGS scalar variance. It is, therefore, plausible to compare the effects of different numerical treatments of the SGS scalar variance first by considering flame configurations that provide the least expected difference in the predicted LES fields.

In the present work, we simplify the chemistry treatment by employing a single mildly-strained steady flamelet obtained from the integration of one-dimensional counter-flow diffusion flame equations with the detailed GRI-Mech 3.0 chemical mechanism. The OPPDIF module of the CHEMKIN package is used to obtain a flamelet solution. Molecular transport properties, such as viscosity and diffusivity, are also obtained from CHEMKIN and are fitted to a power law form in temperature. Instead of forming a flamelet table, we use quadratic B-splines to approximate the flamelet solution for density and temperature [15]. Mean and root mean square values are chosen to be representative statistics since corresponding experimental data are readily available for comparison [24, 25]. We focus mainly on the mixture fraction because of its importance in non-premixed combustion modelling. Many flamelet-based approaches involve the mixture fraction which is used to parametrise chemical composition, molecular properties and enthalpy. And therefore, for accurate predictions of the thermochemical variables, it is a minimal requirement to predict the mixture fraction accurately.

2. Governing equations

2.1. *LES equations*

In the flamelet-based LES approaches for variable-density turbulent flows, the large-scale evolution equations for the resolved density, the density-weighted velocity and the mixture fraction fields are integrated. With a little abuse of notation, these quantities are denoted as $\bar{\rho}$, $\tilde{u}_i$ and $\tilde{\xi}$, respectively. Here, the common Favre notation for the density-weighted resolved quantity is used, i.e. $\tilde{\xi} = \overline{\rho\xi}/\bar{\rho}$, and the bar symbol stands for the resolved (filtered) quantities. The combustion model can be specified through nonlinear functional relationships between the resolved density and thermochemical variables (temperature, species mass fractions) on the one hand, and the resolved mixture fraction $\tilde{\xi}$ and the SGS mixture fraction variance V_ξ on the other. The latter accounts for the effect of the subgrid scale fluctuations of the mixture fraction on the resolved thermochemical variables.

The system of governing equations for the LES model I is written as

$$\frac{\partial \bar{\rho}}{\partial t} + \frac{\partial \bar{\rho}\tilde{u}_j}{\partial x_j} = 0, \tag{1}$$

$$\frac{\partial \bar{\rho}\tilde{u}_i}{\partial t} + \frac{\partial \bar{\rho}\tilde{u}_i\tilde{u}_j}{\partial x_j} = -\frac{\partial \bar{p}}{\partial x_i} + 2\frac{\partial}{\partial x_j}\left[(\bar{\mu}+\mu_T)\left(\widetilde{S}_{ij} - \frac{1}{3}\widetilde{S}_{kk}\delta_{ij}\right)\right], \tag{2}$$

$$\frac{\partial \bar{\rho}\tilde{\xi}}{\partial t} + \frac{\partial \bar{\rho}\tilde{u}_j\tilde{\xi}}{\partial x_j} = \frac{\partial}{\partial x_j}\left[\bar{\rho}(\widetilde{\mathcal{D}}+\mathcal{D}_T)\frac{\partial \tilde{\xi}}{\partial x_j}\right], \tag{3}$$

$$\frac{\partial \bar{\rho}V_\xi}{\partial t} + \frac{\partial \bar{\rho}\tilde{u}_j V_\xi}{\partial x_j} = \frac{\partial}{\partial x_j}\left[\bar{\rho}(\widetilde{\mathcal{D}}+\mathcal{D}_T)\frac{\partial V_\xi}{\partial x_j}\right] - 2\bar{\rho}\widetilde{\chi}_\xi + 2\bar{\rho}(\widetilde{\mathcal{D}}+\mathcal{D}_T)\frac{\partial \tilde{\xi}}{\partial x_j}\frac{\partial \tilde{\xi}}{\partial x_j}, \tag{4}$$

$$\bar{\mu} = \bar{\mu}(\widetilde{T}),\ \ \bar{\rho}\widetilde{\mathcal{D}} = \bar{\rho}\widetilde{\mathcal{D}}(\widetilde{T}),\ \ \mu_T = \rho C_S\Delta^2(2\widetilde{S}_{ij}\widetilde{S}_{ij})^{1/2},\ \ \bar{\rho}D_T = \mu_T/Sc_T \tag{5}$$

$$\bar{\rho} = \bar{\rho}(\tilde{\xi}, V_\xi),\ \ \widetilde{T} = \widetilde{T}(\tilde{\xi}, V_\xi), \tag{6}$$

where $\bar{p}$, $\widetilde{S}_{ij}$ and $\widetilde{\chi}_\xi$ are the resolved pressure, strain rate and scalar dissipation rate, respectively. In the LES momentum equation (Equation 2), the Smagorinsky model is employed to obtain the deviatoric part of the unclosed SGS stress $\tau_{ij} = \bar{\rho}\tilde{u}_i\tilde{u}_j - \bar{\rho}\widetilde{u_iu}_j$, i.e. $\tau_{ij} - \delta_{ij}\tau_{kk}/3 = 2\mu_T(\widetilde{S}_{ij} - \delta_{ij}\widetilde{S}_{kk}/3)$. Here, μ_T is the turbulent eddy viscosity with a model constant C_S which is computed according to the Germano dynamic procedure [35] with Lilly's modification [36]. In addition, a commonly used averaging operation in the periodic direction is employed for the numerator and denominator in the expression for C_S. In both scalar equations (Equations 3 and 4), the unclosed subgrid scalar flux is modelled by a standard gradient diffusion hypothesis with the same subgrid diffusivity $\bar{\rho}\mathcal{D}_T$ for both scalar fields, for example $\bar{\rho}\tilde{u}_i\tilde{\xi} - \bar{\rho}\widetilde{u_i\xi} = \bar{\rho}\mathcal{D}_T\partial\tilde{\xi}/\partial x_i$. The subgrid diffusivity $\bar{\rho}D_T$ is specified based on the eddy viscosity and the subgrid Schmidt number as shown by Equation (5), with a commonly used value of $Sc_T = 0.4$ [26]. Finally, the unclosed scalar dissipation rate term $2\bar{\rho}\widetilde{\chi}_\xi$ requires modelling as well.

A standard way to model the scalar dissipation rate term is to decompose it into resolved and SGS parts where the latter is taken to be proportional to the SGS mixture fraction variance [22,33]:

$$2\overline{\rho\mathcal{D}|\nabla\xi|^2} = 2\bar{\rho}\widetilde{\chi}_\xi = 2\bar{\rho}\widetilde{\mathcal{D}}\frac{\partial \tilde{\xi}}{\partial x_j}\frac{\partial \tilde{\xi}}{\partial x_j} + C\frac{\bar{\rho}\mathcal{D}_T V_\xi}{\Delta^2}, \tag{7}$$

where C is a model constant chosen to be $C = 2$, and Δ is the characteristic turbulence resolution scale. Substitution of Equation (7) into Equation (4) results in the final form of the governing equations for the SGS variance.

2.2. *SGS variance equations*

To distinguish further between the two models we denote by V_ξ^{I} a solution of the SGS variance equation (Equation 4) (model I), and by V_ξ^{II} the SGS variance that is obtained from model II. Introducing for brevity the operator $\mathcal{L}$ defined as $\mathcal{L}(\cdot) \equiv \widetilde{\mathrm{D}}(\cdot)/\widetilde{\mathrm{D}}t - \partial/\partial x_j(\bar{\rho}(\widetilde{\mathcal{D}} + \mathcal{D}_T)\partial(\cdot)/\partial x_j)$ with the total derivative $\widetilde{\mathrm{D}}/\widetilde{\mathrm{D}}t \equiv \bar{\rho}\partial/\partial t + \bar{\rho}\widetilde{u}_j\partial/\partial x_j$, it follows from

Equations (4) and (7) that V_ξ^{I} evolves by

$$\mathcal{L}\left(V_\xi^{\mathrm{I}}\right) = 2\bar{\rho}\mathcal{D}_T\left(\frac{\partial\tilde{\xi}}{\partial x_j}\right)^2 - \frac{C\bar{\rho}\mathcal{D}_T}{\Delta^2}V_\xi^{\mathrm{I}}. \tag{8}$$

In model II, instead of solving the transport equation (Equation 4) for V_ξ, we solve an equation for $S_\xi \equiv \widetilde{\xi^2}$ directly [21], and then compute V_ξ^{II} from $\tilde{\xi}$ and S_ξ as $V_\xi^{\mathrm{II}} = S_\xi - (\tilde{\xi})^2$. The equation for S_ξ can be readily deduced from the corresponding continuity and mixture fraction equations and, with the scalar dissipation rate model given by Equation (7), it can be written as

$$\mathcal{L}(S_\xi) = -2\bar{\rho}\widetilde{\mathcal{D}}\left(\frac{\partial\tilde{\xi}}{\partial x_j}\right)^2 - \frac{C\bar{\rho}\mathcal{D}_T}{\Delta^2}V_\xi^{\mathrm{II}}, \tag{9}$$

with

$$V_\xi^{\mathrm{II}} = S_\xi - (\tilde{\xi})^2. \tag{10}$$

We note that Equation (4) is equivalent to Equations (9) and (10) at the level of partial differential equations, and thus they have identical solutions V_ξ^{I} and V_ξ^{II} given a consistent set of the corresponding boundary and initial conditions. Furthermore, it is seen that both equations appear to be in the same functional form. In particular, both equations contain the squared-gradient source term on the right-hand side, which differs in terms of the sign and the diffusivity coefficient. In model I the positive squared-gradient term $2\bar{\rho}\mathcal{D}_T|\nabla\tilde{\xi}|^2$ is responsible for the production of the SGS variance, while in model II the corresponding term $-2\bar{\rho}\widetilde{\mathcal{D}}|\nabla\tilde{\xi}|^2$ is negative and results in dissipation of the SGS variance.

In the LES literature, model II is often viewed as the better alternative due to the absence of the production term, which can be a potential source of numerical errors stemming from an underresolved discrete representation of the squared-gradient term in practical LES [18,20]. However, as may be seen from Equation (9), model II would also be subject to numerical errors associated with the underresolution of the squared-gradient term as soon as the resolved dissipation rate is represented by any model which employs decomposition and contains the dissipation rate of the resolved field $2\bar{\rho}\widetilde{\mathcal{D}}|\nabla\tilde{\xi}|^2$ as in Equation (7). On the other hand, the sensitivity effect due to underpredicting the squared-gradient term is opposite for models I and II, which can be seen from the following equivalent form of model II written as

$$\mathcal{L}\left(V_\xi^{\mathrm{II}}\right) = -2\bar{\rho}\widetilde{\mathcal{D}}\left(\frac{\partial\tilde{\xi}}{\partial x_j}\right)^2 - \mathcal{L}(\tilde{\xi}^2) - \frac{C\bar{\rho}\mathcal{D}_T}{\Delta^2}V_\xi^{\mathrm{II}}. \tag{11}$$

Qualitatively, since the dissipation term on the right-hand side of Equation (11) appears with a negative sign, the underprediction of the squared-gradient term tends to increase values of V_ξ^{II} due to less dissipative action. In model I this results in the underprediction of the production term, which decreases the SGS variance V_ξ^{I}.

The arguments in favour of model II usually involve an appeal to coarse grids (i.e. large filter widths) and high Reynolds numbers, so one could assume that the values of the subgrid diffusivity are much higher compared to the values of its molecular counterpart. In such situations, it might be reasonable to treat the resolved dissipation term of model II

$(2\bar{\rho}\widetilde{\mathcal{D}}|\nabla\tilde{\xi}|^2)$ as a rather unimportant source of errors contrary to that role of the production term of model I $(2\bar{\rho}\mathcal{D}_T|\nabla\tilde{\xi}|^2)$. In this regard, we remark that in combustion problems molecular transport properties are greatly enhanced by the exothermicity of chemical reactions so the molecular diffusivity could be locally comparable to or exceed the corresponding subgrid diffusivity. In addition, in practical combustion LES, it is often a necessity to use relatively fine grids and small filter widths in some parts of the computational domain to capture the important flow features (for example, the development of jet mixing layers). This is certainly the case for high-fidelity LES. Therefore, as the LES grid becomes finer and the turbulent subgrid diffusivity values decrease on the one hand, and the values of the molecular diffusivity increase on the other, traditional arguments based on the relative importance of the production and resolved dissipation terms become less convincing.

Another frequently invoked argument in favour of model II is the ability to recover the exact maximum value of the SGS variance when the scalar dissipation rate is neglected [20]. It can be seen from Equation (9) that if the scalar dissipation rate is set to zero then the resolved square of the mixture fraction $\widetilde{\xi^2}$ and the resolved mixture fraction $\tilde{\xi}$ both satisfy the same transport equation, i.e. $\mathcal{L}(\widetilde{\xi^2}) = 0$ and $\mathcal{L}(\tilde{\xi}) = 0$. As a result, one might conclude that $\widetilde{\xi^2}$ and $\tilde{\xi}$ evolve identically $(\widetilde{\xi^2} = \tilde{\xi})$, which formally leads to the maximum value of the SGS variance, $V_\xi = \widetilde{\xi^2} - \tilde{\xi}^2 = \tilde{\xi} - \tilde{\xi}^2 = \tilde{\xi}(1-\tilde{\xi}) = V_\xi^{\max}$ [20]. However, this reasoning appears to be fallacious. First, from the basic property of the mixture fraction field, i.e. $0 \le \xi \le 1$, it follows that $\widetilde{\xi^2} \le \tilde{\xi}$. In particular, the equality takes place only when $\tilde{\xi} = 0$ or $\tilde{\xi} = 1$. Second, despite the exact functional form of the transport equations for $\widetilde{\xi^2}$ and $\tilde{\xi}$ the corresponding solutions would still be different because there are always different boundary conditions for these fields which have to be prescribed for consistency (except for the trivial cases of zero and unity values). As a result, when the scalar dissipation rate is neglected model II reproduces the trivial result of zero SGS variance.

At the discrete level, however, the solutions V_ξ^{I} and V_ξ^{II} differ because the numerical approximation errors involved in the two approaches differ. To identify the origin of these errors it is convenient to rewrite Equation (11) in yet another equivalent form which enables term-by-term comparison with model I:

$$\mathcal{L}\left(V_\xi^{\mathrm{II}}\right) = 2\bar{\rho}\mathcal{D}_T\left(\frac{\partial\tilde{\xi}}{\partial x_j}\right)^2 - \left[\mathcal{L}(\tilde{\xi}^2) + 2\bar{\rho}(\widetilde{\mathcal{D}} + \mathcal{D}_T)\left(\frac{\partial\tilde{\xi}}{\partial x_j}\right)^2\right] - \frac{C\bar{\rho}\mathcal{D}_T}{\Delta^2}V_\xi^{\mathrm{II}}. \tag{12}$$

Before proceeding with the analysis it is remarked that this form of the SGS variance equation is not actually solved at the discrete level in model II, it is invoked here to delineate the differences between the two models. It is seen that models I and II are indeed identical if the second term on the right-hand side of Equation (12) is equal to zero. This is always true at the continuous level since it represents a conservation law for the square of the resolved mixture fraction:

$$\mathcal{L}(\tilde{\xi}^2) + 2\bar{\rho}(\widetilde{\mathcal{D}} + \mathcal{D}_T)\left(\frac{\partial\tilde{\xi}}{\partial x_j}\right)^2 = 0. \tag{13}$$

At the discrete level the situation is different. While for model I the discrete version of this conservation law is always satisfied by virtue of the formulation, it is not the case for model II. Clearly, adopting model II would be equivalent to the evaluation of the expression $\mathcal{L}(\tilde{\xi}^2) + 2\bar{\rho}(\widetilde{\mathcal{D}} + \mathcal{D}_T)|\nabla\tilde{\xi}|^2$ directly at the discrete level by the substitution of $(\tilde{\xi})^2$ obtained from the discrete mixture fraction (a solution of the discrete version of the mixture fraction

equation $\mathcal{L}(\tilde{\xi}) = 0$). Thus, the expression $\mathcal{L}(\tilde{\xi}^2) + 2\bar{\rho}(\widetilde{\mathcal{D}} + \mathcal{D}_T)|\nabla\tilde{\xi}|^2$ would not necessarily need to be zero. As a result, if one adopts model II then a conservation law for $(\tilde{\xi})^2$, i.e. Equation (13), is not enforced at the discrete level which leads to an additional source of numerical errors. In other words, a visible disadvantage in the formulation of model II stems from the implied lack of conservation of the square of the resolved mixture fraction field (Equation 13) caused by the subtraction of $(\tilde{\xi})^2$ in Equation (10) at the discrete level.

To fix these ideas it is instructive to consider the discrete versions of Equations (8) and (12). Let $\Omega_{h,\tau}$ be the temporal–spatial discretisation of the computational domain $\Omega \times T$ where an LES problem (Equations 1–6) is considered, i.e. $\Omega_{h,\tau} = \{(\mathbf{x}_m, t^n) : \mathbf{x}_m \in G_h; t^n \in T_\tau\}$. Here, $G_h \equiv \{\mathbf{x}_1, \ldots, \mathbf{x}_M\}$ and $T_\tau \equiv \{0 \le t_1, \ldots, t_N \le T\}$ are spatial and temporal grids, respectively. Let us further denote by L_h and G_h the discrete representations of the operator $\mathcal{L}(\cdot)$ and the gradient operator $\nabla(\cdot)$, which depend on the adopted numerical/discretisation scheme. Thus, as the discrete analogue of Equation (8) we solve for the approximate solution V_h^{I} defined on $\Omega_{h,\tau}$ the following equation:

$$\mathrm{L}_h\left(V_h^{\mathrm{I}}\right) = 2\bar{\rho}_h\mathcal{D}_{T,h}\left(\mathrm{G}_h(\tilde{\xi}_h)\right)^2 - \frac{C\bar{\rho}_h\mathcal{D}_{T,h}}{\Delta^2}V_h^{\mathrm{I}}, \tag{14}$$

where $\bar{\rho}_h$, $\mathcal{D}_{T,h}$ are the discrete density and turbulent diffusivity, respectively, and a discrete approximation of the mixture fraction $\tilde{\xi}_h$ is a solution of $\mathrm{L}_h(\tilde{\xi}_h) = 0$. Note that all discrete variables are functions of not only the local grid resolution h but also the turbulent resolution scale Δ, i.e. $\tilde{\xi}_h(\Delta)$, $\bar{\rho}_h(\Delta)$, and so on. In this work Δ is taken to be equal to h, or $h/\Delta = 1$ which is a standard choice in practical LES, so the dependence on h is two-fold. If the exact LES fields on the discrete domain $\Omega_{h,\tau}$ are denoted by $\tilde{\xi}_{m,n} = \tilde{\xi}(\mathbf{x}_m, t^n)$, $\bar{\rho}_{m,n} = \bar{\rho}(\mathbf{x}_m, t^n)$, $V_{m,n}^{\mathrm{I}} = V_\xi^{\mathrm{I}}(\mathbf{x}_m, t^n)$, $\tilde{\xi}_{m,n} = \tilde{\xi}(\mathbf{x}_m, t^n)$, etc., then one can define the discretisation (local) error R_h^{I} for model I by substitution the exact discrete variance $V_{m,n}^{\mathrm{I}}$ into Equation (14) to obtain

$$R_h^{\mathrm{I}} = 2\bar{\rho}_h\mathcal{D}_{T,h}\left(\mathrm{G}_h(\tilde{\xi}_h)\right)^2 - \frac{C\bar{\rho}_h\mathcal{D}_{T,h}}{\Delta^2}V_{m,n}^{\mathrm{I}} - \mathrm{L}_h\left(V_{m,n}^{\mathrm{I}}\right). \tag{15}$$

For the second-order scheme considered in this work $R_h^{\mathrm{I}} = O(h^2 + \tau^2)$ with τ being a time step. Note that the approximation error for the SGS variance of model I ϵ_h^{I}, which is defined according to $V_h^{\mathrm{I}} = V_{m,n}^{\mathrm{I}} + \epsilon_h^{\mathrm{I}}$, satisfies

$$\mathrm{L}_h\left(\epsilon_h^{\mathrm{I}}\right) = R_h^{\mathrm{I}} - \frac{C\bar{\rho}_h\mathcal{D}_{T,h}}{\Delta^2}\epsilon_h^{\mathrm{I}}, \tag{16}$$

which follows from its definition and Equations (14) and (15). Similarly to Equation (14), the discrete analogue of model II (Equation 12) can be written as

$$\mathrm{L}_h\left(V_h^{\mathrm{II}}\right) = 2\bar{\rho}_h\mathcal{D}_{T,h}\left(\mathrm{G}_h(\tilde{\xi}_h)\right)^2 - r_h - \frac{C\bar{\rho}_h\mathcal{D}_{T,h}}{\Delta^2}V_h^{\mathrm{II}}, \tag{17}$$

where r_h is defined as

$$r_h \equiv \mathrm{L}_h\left(\tilde{\xi}_h^2\right) + 2\bar{\rho}_h(\widetilde{\mathcal{D}}_h + \mathcal{D}_{T,h})\left(\mathrm{G}_h(\tilde{\xi}_h)\right)^2, \tag{18}$$

and represents the difference between the discrete variance equations of models I and II. Clearly, it is not equal to zero since $(\tilde{\xi}_h)^2$ being evaluated directly from the solution of

$\mathrm{L}_h(\tilde{\xi}_h) = 0$ does not satisfy to the discrete analogue of Equation (13), which is given by

$$\mathrm{L}_h(s_h) + 2\bar{\rho}_h(\widetilde{\mathcal{D}}_h + \mathcal{D}_{T,h})\big(\mathrm{G}_h(\tilde{\xi}_h)\big)^2 = 0. \tag{19}$$

Here, the solution s_h is the discrete representation of the square of the resolved mixture fraction $s_\xi \equiv (\tilde{\xi})^2$. We further note that the term r_h does not involve the constant C used in modelling the subgrid part of the resolved scalar dissipation rate (Equation 7), which suggests that the difference between models I and II is not related to a particular form of the scalar dissipation rate model, as long as it is represented by the decomposition into the resolved and subgrid parts. Clearly, one could prescribe an ideal dissipation rate model by choosing some general coefficient $C(\mathbf{x}, t)$ in such a way that Equation (7) is satisfied exactly. Nevertheless, it would affect neither r_h nor, as a result, the differences between the discrete SGS variances.

From comparison of Equations (14) and (17) we observe that given an identical set of the corresponding boundary and initial conditions both discrete variances will evolve identically if r_h is zero, i.e.

$$V_h^{\mathrm{II}} = V_h^{\mathrm{I}}, \quad \text{if } \mathrm{L}_h\left(\tilde{\xi}_h^2\right) + 2\bar{\rho}_h(\widetilde{\mathcal{D}}_h + \mathcal{D}_{T,h})\big(\mathrm{G}_h(\tilde{\xi}_h)\big)^2 = 0. \tag{20}$$

Furthermore, qualitatively it is seen that locally and for small times, the difference between the discrete SGS variances V_h^{I} and V_h^{II} will be governed by the sign of r_h according to

$$V_h^{\mathrm{II}} > V_h^{\mathrm{I}}, \quad \text{if } \mathrm{L}_h(\tilde{\xi}_h^2) + 2\bar{\rho}_h(\widetilde{\mathcal{D}}_h + \mathcal{D}_{T,h})\big(\mathrm{G}_h(\tilde{\xi}_h)\big)^2 < 0, \tag{21}$$

$$V_h^{\mathrm{II}} < V_h^{\mathrm{I}}, \quad \text{if } \mathrm{L}_h(\tilde{\xi}_h^2) + 2\bar{\rho}_h(\widetilde{\mathcal{D}}_h + \mathcal{D}_{T,h})\big(\mathrm{G}_h(\tilde{\xi}_h)\big)^2 > 0. \tag{22}$$

In particular, it is noted that even if initially both variances coincide and the discrete mixture fraction $\tilde{\xi}_h$ is such that r_h equals zero, a small underprediction in the values of the resolved gradient $\mathrm{G}_h(\tilde{\xi}_h)$ would result in negative values of r_h which, in turn, would promote higher values of the discrete SGS variance V_h^{II} compared to those of V_h^{I} due to less dissipation provided by the extra source term r_h. A similar trend was observed by Kaul *et al.* [20] in a priori analysis of the DNS data of homogeneous and isotropic turbulence and attributed to the underprediction of V_h^{I} due to numerical errors caused by the chain-rule approximation.

The extra numerical error source term r_h of the discrete model II can be further simplified by subtracting Equation (19) from Equation (18). If we denote by $\epsilon_h = \tilde{\xi}_h - \tilde{\xi}_{m,n}$ and $\epsilon_h^s = s_h - \tilde{\xi}_{m,n}^2$, the corresponding approximation errors of the mixture fraction and the square of the mixture fraction, respectively, then r_h takes form

$$\begin{aligned} r_h = \mathrm{L}_h\left(\tilde{\xi}_h^2 - s_h\right) &= \mathrm{L}_h\left(\tilde{\xi}_{m,n}^2 + 2\tilde{\xi}_{m,n}\epsilon_h + \epsilon_h^2 - \tilde{\xi}_{m,n}^2 - \epsilon_h^s\right) \\ &= \mathrm{L}_h\left(2\tilde{\xi}_h\epsilon_h - \epsilon_h^2\right) - \mathrm{L}_h\left(\epsilon_h^s\right). \end{aligned} \tag{23}$$

From this equation it is seen that the discrete solution V_h^{II} will be affected non-trivially by the extra source term r_h which evolves (to the leading order) as $r_h \approx \mathrm{L}_h(2\tilde{\xi}_h\epsilon_h) - \mathrm{L}_h(\epsilon_h^s)$. This is not the case for the discrete SGS variance of model I. Specifically, this inability to enforce the conservation of the square of the resolved mixture fraction at the discrete level makes model II less attractive on pure formulation grounds.

It is well appreciated that the accuracy of an LES solution depends on (i) the grid resolution, (ii) the numerical/discretisation method, and (iii) the SGS models. There is

always a trade-off between numerical resolution h and resolution of the turbulent motions Δ. Larger values of Δ allow better numerical resolution but worse resolution of the smaller-scale turbulent motions. The more 'optimal' choice of the turbulent resolution scale Δ, such as the one taken in this work ($h/\Delta = 1$), could lead to simulations that are subject to significant numerical errors. Furthermore, both numerical and SGS modelling errors interact non-trivially and are difficult to separate; so it may or may not be that there is a cancellation between them (for example, between r_h and errors originating from the SGS part of the scalar dissipation rate model given by $C\bar{\rho}_h \mathcal{D}_{T,h} V_h^{\mathrm{II}}/\Delta^2$), but it is the overall observable error which is important.

Hence, it is appropriate to study models in the presence of the numerical errors, and the purpose of the present paper is to study how the numerical difference between the two models $r_h(\Delta)$ affects the SGS variances $V_h^{\mathrm{I}}(\Delta)$ and $V_h^{\mathrm{II}}(\Delta)$ and, as a result, the overall LES solution with respect to the turbulence resolution scale Δ. Thus, in this study we pursue a rather narrow objective by focusing on the different implementations of the SGS variance, rather than studying the effects of the SGS models themselves which are chosen to be quite standard and widely used. As a result, we use the word 'model' in a general sense here since at the continuous level both models are described by the equivalent set of partial differential equations and, therefore, their exact solutions are identical. In summary, we refer to Equations (1)–(3), (5), (8) as model I and Equations (1)–(3), (5), (9), (10) as model II, respectively.

2.3. *Combustion model equations*

A combustion model and transport properties given by Equations (5) are obtained from a steady laminar flamelet solution with the detailed GRI-Mech 3.0 chemical mechanism. A mildly-strained flamelet solution with a nominal strain rate of $a = 50\ \mathrm{s}^{-1}$ is computed in a 1D counter-flow configuration by the OPPDIF module of CHEMKIN 4.1. The full details of the combustion model specification can be found elsewhere [15]. Here, we briefly summarise the main assumptions and resulting equations.

The specific volume $v = \rho^{-1}$ is approximated by fitting a quadratic B-spline $v_s(\xi)$ to the flamelet solution $v(\xi)$. In its simplest form a quadratic B-spline approximation is represented by a single quadratic function $v_o(\xi) = a + b\xi + c\xi^2$ which translates to the following expression for the resolved specific volume $\widetilde{v}_o(\tilde{\xi}, V_\xi) = a + b\tilde{\xi} + c\widetilde{\xi^2} = a + b\tilde{\xi} + c(\tilde{\xi}^2 + V_\xi)$. Here, the coefficients a, b and c can be found by fitting to the CHEMKIN flamelet data for specific volume. In this work, we consider a quadratic B-spline approximation $v_s(\xi)$ consisting of three parabolic pieces to approximate the flamelet solution $v(\xi)$, and define the resolved specific volume, and therefore the resolved density, as

$$\widetilde{v}(\tilde{\xi}, V_\xi) = v_s(\tilde{\xi}) \frac{\widetilde{v}_o(\tilde{\xi}, V_\xi)}{\widetilde{v}_o(\tilde{\xi}, 0)}, \quad \bar{\rho}(\tilde{\xi}, V_\xi) = \widetilde{v}^{-1}(\tilde{\xi}, V_\xi). \tag{24}$$

This model yields the relations

$$\widetilde{v}(\tilde{\xi}, 0) = v_s(\tilde{\xi}), \tag{25}$$

$$\frac{\widetilde{v}(\tilde{\xi}, V_\xi)}{\widetilde{v}(\tilde{\xi}, 0)} = \frac{\widetilde{v}_o(\tilde{\xi}, V_\xi)}{\widetilde{v}_o(\tilde{\xi}, 0)}, \tag{26}$$

and indeed these relations are the motivation for the model. Note that $\widetilde{v}_o(\tilde{\xi}, V_\xi)$ is known in terms of $\tilde{\xi}$ and V_ξ, whereas the exact value of $\widetilde{v}$ depends on the PDF of the mixture fraction, not solely on its mean and variance. Similar expressions are applied to other thermochemical variables [15].

The functional dependence of the mixture molecular viscosity and mixture fraction diffusivity on temperature are also computed from CHEMKIN and its thermal and transport databases, and then cast in a power-law form given by

$$\mu(T) = 1.75 \times 10^{-5} \left(\frac{T}{T_0}\right)^{0.69} \frac{\text{kg}}{\text{m} \cdot \text{s}}, \quad \rho D(T) = 2.48 \times 10^{-5} \left(\frac{T}{T_0}\right)^{0.72} \frac{\text{kg}}{\text{m} \cdot \text{s}}, \quad (27)$$

with $T_0 = 298$ K.

2.4. *LES derived statistics*

Following the framework introduced by Pope [7], the LES generated statistics can be decomposed into two components $Q^m(\Delta) = Q^W(\Delta) + Q^r(\Delta)$, where $Q^W(\Delta)$ is defined solely by the resolved LES fields, while $Q^r(\Delta)$ estimates the contribution from the residual (subgrid) fields and can depend on both resolved and residual LES fields. Then, the predictive capabilities of LES models can be estimated in terms of overall accuracy and cost based on how good $Q^m(\Delta)$ approximates the true DNS statistic Q, and how fast $Q^m(\Delta)$ converges to its asymptotic value with respect to Δ. Note that if the experimental statistic Q_{exp} is available, say from high-resolution experiments, it still may differ from the true statistic Q due to experimental uncertainties on the one hand and combustion modelling limitations (flamelet assumption, simplified molecular transport, etc.) on the other.

The specification of Q^r is challenging because of the unknown residual fields. It also depends on the particular statistics considered. In the present work we employ and test two simple estimates of Q^r when the statistic of interest Q is taken to be the mean or the variance of the mixture fraction field. If Q is the statistical mean, i.e. $Q = \langle\xi\rangle$, then $Q = \langle\xi\rangle = \langle\tilde{\xi}\rangle + \langle\xi''\rangle$, where ξ'' is defined by the decomposition $\xi = \tilde{\xi} + \xi''$. Thus, one can take Q^W as the mean of the resolved mixture fraction field $Q^W = \langle\tilde{\xi}\rangle$ and $Q^r = \langle\xi''\rangle = 0$. This leads to the following estimate – $Q \approx Q^m = Q^W + Q^r = Q^W = \langle\tilde{\xi}\rangle$. Note that the approximation $Q^r = \langle\xi''\rangle \approx 0$ is reasonable in free-shear flows if the LES grid provides an adequate resolution. If an LES grid is not fine enough then a model for $Q^r = \langle\xi''\rangle$ has to be specified.

In the case where the variance $Q = \langle\xi^2\rangle - \langle\xi\rangle^2$, the residual contribution is important and can be modelled by the mean SGS variance $Q^r = \langle V_\xi\rangle$. This follows from the expansion of Q in terms of $\tilde{\xi}$ and ξ'' and the assumption that $\langle\xi''\rangle \approx 0$, and leads to $Q \approx \langle(\tilde{\xi})^2\rangle - \langle\tilde{\xi}\rangle^2 + \langle 2\tilde{\xi}\xi'' + \xi''^2\rangle$. The first two terms produce the resolved LES variance while the last ones can be approximated by $\langle V_\xi\rangle$. Thus, the LES-based estimation for the variance is written as $Q^m = Q^W + Q^r = [\langle(\tilde{\xi})^2\rangle - \langle\tilde{\xi}\rangle^2] + \langle V_\xi\rangle$. Note that the present model is a reasonable estimation for the variance as soon as the mean mixture fraction is adequately resolved, i.e. the assumption that $\langle\xi''\rangle \approx 0$ is valid throughout the flow domain.

In summary, a primary objective of the present work is to study how the 'minimally' different, i.e. at the discrete level, LES models I and II affect both components of the total LES statistics with respect to the turbulence resolution scale Δ.

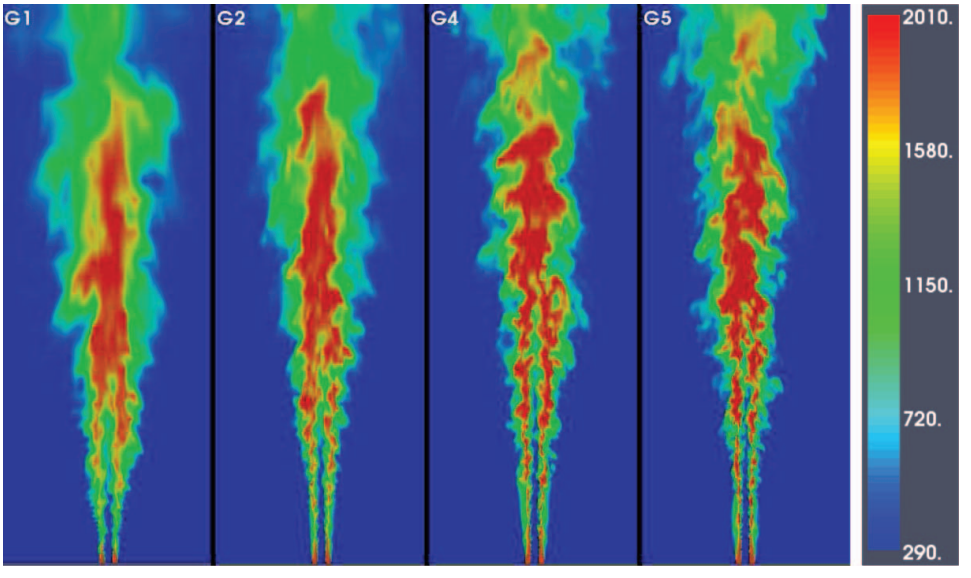

Figure 1. Geometrical configuration of Sandia flame D visualised by instantaneous temperature contours on different grids $G1$, $G2$, $G4$ and $G5$. The cold (blue) methane–air mixture jet that emanates from the bottom is ignited, stabilised by the hot pilot products (red), and then burns further downstream. The colour bar gives the temperature in Kelvin.

3. Computational configuration

Sandia flame D has been studied quite extensively in the experimental works of Barlow and Frank [24] and Schneider *et al.* [25], and is visualised in Figure 1 by temperature contours on several grids with increased resolution. Qualitatively, it is readily seen that as the grid resolution increase the finer scale structures become more and more apparent, thus showing the dependence of the LES solution on the turbulence resolution scale. The fuel jet consists of a mixture of 25% methane and 75% air (by volume) and emanates from a nozzle (located at the bottom in Figure 1) with diameter $D = 7.2\,\mathrm{mm}$ at a bulk velocity of $U_\mathrm{b} = 49.6\,\mathrm{m\,s^{-1}}$ and temperature of 294 K. The nozzle is surrounded by a coaxial pilot nozzle with diameter of $2.62D$. The hot pilot flow is a lean burnt mixture of C_2H_2, air, CO_2, H_2 and N_2 corresponding to a mixture fraction value of $\xi = 0.271$, with a bulk velocity of $11.4\,\mathrm{m\,s^{-1}}$ and temperature of 1880 K. The coaxial burner is further surrounded by co-flowing air with a bulk velocity of $0.9\,\mathrm{m\,s^{-1}}$ and temperature of 291 K. A characteristic Reynolds number of Re = 22,400 is defined based on the fuel jet velocity, kinematic viscosity ($\nu = 1.58 \times 10^{-5}\,\mathrm{m^2\,s^{-1}}$) and the nozzle diameter. At this Reynolds number the flame is characterised by a minimal level of local extinction due to moderate strain rates exerted by the velocity field.

In this work the computational and geometrical configurations follow closely those reported in a recent study of Sandia flame D by Kemenov and Pope [15]. Here, for completeness we briefly highlight the main parameters and conditions used in the performed simulations. The computational domain is a cylinder with an extent of $120.3D \times 20D \times 2\pi$ represented in cylindrical coordinates (x, r, θ). The jet and pilot nozzles have a small axial extension of $0.3D$ upstream of the nozzle exit plane, which is taken as the origin of the axial coordinate, x. The dimensions of the computational domain as well as flow variables

are non-dimensionalised by the characteristic jet parameters (i.e. diameter, bulk velocity, density).

An accurate specification of the inflow boundary condition is notoriously difficult for this type of flame configuration. Vreman *et al.* [30], for example, observed a significant decrease in the centreline mixture fraction if the experimental values of the mean and *rms* fields are specified at the nozzle exit plane ($x = 0$). As a result, the authors proposed to use the inflow conditions at the $x = D$ inlet plane that demonstrated an accurate match between the computed mean centreline mixture fraction and the corresponding experimental data, even though the mean centreline velocity appeared to be quite overpredicted downstream. This trend manifested by overprediction of the mean centreline velocity downstream, after $x = 20D$, was observed in other LES flame D studies [26, 27] which employed different methods for specification of the inflow condition. Clayton and Jones [31], on the other hand, advocated the use of turbulence-free inflow conditions with zero fluctuations on the grounds that the measured turbulent intensities of the jet ($\sim 3\%$) are much smaller than those generated in the jet mixing layers further downstream.

In this work, following Ihme and Pitsch [22], we generate the turbulent jet inflow velocity condition by separately running a high resolution LES of the stationary turbulent pipe flow where the experimental mean and *rms* axial velocity profiles as measured by the TU Darmstadt group [25] are enforced. The turbulent pipe flow simulation has been conducted on a $192 \times 96 \times 96$ grid with periodic boundary conditions in the streamwise direction. Accumulated velocity field data are saved and used to generate inflow conditions by linear interpolation onto the LES grid at the jet inlet plane ($x = -0.3D$). It was also observed that shifting the inlet plane further upstream leads to excessive velocity fluctuations on the jet centreline, especially for coarse grids, and, as a result, to an inability to match the mean velocity experimental profiles at the nozzle exit plane in the centreline region. The inflow velocity condition for the pilot is based on the measured mean with superimposed uncorrelated random noise fluctuations of low intensity ($\sim 1\%$) according to the measured *rms* profiles, while in the co-flow region the measured bulk values with zero turbulent intensity are used. The mixture fraction field is prescribed as a step function according to an experimental value of $\tilde{\xi} = 0.271$ for the pilot, and $\tilde{\xi} = 1$ and $\tilde{\xi} = 0$ for the jet and co-flow, respectively. Finally, convective boundary conditions are employed for velocity and scalar fields on the outflow boundary including the entrainment boundary of the computational domain.

A structured Stanford LES code is employed to solve the variable-density LES equations written in cylindrical coordinates [11]. The numerical method is second-order accurate in space and time and adopts an energy-conserving discretisation scheme for the momentum equation. Scalar transport equations are discretised using the QUICK scheme [37] and solved employing a semi-implicit iterative technique, which has proven to be effective for typical low-Mach combustion problems [11, 22]. Domain decomposition is used for the LES code parallelisation.

It is seen from Equations (1)–(5) that the LES solution is a function of the turbulent resolution scale $\Delta(\boldsymbol{x})$. As is customarily done in practice, we associate the turbulent resolution scale with the local numerical grid resolution $h(\boldsymbol{x})$, thus enforcing $h(\boldsymbol{x})/\Delta(\boldsymbol{x}) = 1$. In this work we employ five grids $G1, \ldots, G5$ with a progressively increasing resolution from about 0.2 to 10.5 million cells as detailed in Table 1. All grids are stretched in the axial direction as well as in the radial direction, with clustering in the jet nozzle and pilot annulus regions, while remaining uniformly spaced in the circumferential direction. Grid resolution parameters for the jet nozzle and the pilot are given in Table 2. The dependence of the grid cell sizes with respect to distance in the radial and axial directions is shown

Table 1. Grid parameters and the minimum/maximum cell width in the non-dimensionalised axial and radial directions $\hat{x} \equiv x/D$, $\hat{r} \equiv r/D$.

Grid	Resolution $(\hat{x}, \hat{r}, \theta)$	Cells, 10^6	$\Delta^x_{\min}$	$\Delta^x_{\max}$	$\Delta^r_{\min}$	$\Delta^r_{\max}$
G1	$96 \times 64 \times 32$	0.196	$12. \times 10^{-2}$	4.78	2.8×10^{-2}	1.96
G2	$160 \times 96 \times 64$	0.983	7.3×10^{-2}	2.89	1.8×10^{-2}	1.33
G3	$256 \times 128 \times 64$	2.097	4.5×10^{-2}	1.81	1.4×10^{-2}	1.01
G4	$256 \times 192 \times 96$	4.719	4.5×10^{-2}	1.81	9.4×10^{-3}	0.67
G5	$320 \times 256 \times 128$	10.485	3.6×10^{-2}	1.45	7.0×10^{-3}	0.51

in Figures 2(*a*) and (*b*) and compared to the spatial resolution size of 0.75 mm achieved in the scalar measurements [24]. It is seen that the finest grid $G5$ provides the resolution comparable to the experimental one, or better, only in the near-field region of $x \leq 6.5D$ and $r \leq 4.5D$ which rapidly shrinks with grid coarsening. Due to approximately linear stretching, the axial grid spacing grows downstream. For example, at an axial location of $x = 15D$, the axial resolution is approximately twice the experimental resolution on the $G5$ grid and as high as seven times the experimental value on the coarsest $G1$ grid. At that location the jet's edge is at about $3D$ in the radial direction so the radial grid spacing of the first three grids $G1$–$G3$ is larger than the experimental resolution with $G1$'s being the largest and approximately two and a half times larger than the size of the experimental probe volume.

In all simulations, with the exception of the finest grid $G5$, a zero state is employed as the initial condition for all scalar variables except the axial velocity field, which is taken to be uniform and equal to the co-flow velocity in the whole domain. For the finest grid, the initial fields are interpolated from a statistically-stationary solution on the preceding grid $G4$. Time integration is performed with a variable time step corresponding to a CFL number of 0.3–0.35. Statistics are accumulated after the simulation has reached a statistically-stationary state which is verified by convergence in the *rms* statistics. This corresponds to about 10 flow-through times based on the jet averaged centreline velocity and the characteristic length of $L = 75D$ ($t_{fl} = \int_0^L \mathrm{d}x/\langle\widetilde{U}\rangle(x, 0)$). Such a defined flow-through time is about twice as large as a time computed one based on the bulk velocity value ($t_\mathrm{B} = L/U_\mathrm{B}$). After that, the simulation is continued for approximately five flow-through times to accumulate statistics. LES statistics Q^m are computed by averaging in time and the circumferential direction and, thus, are functions of x and r. These averages are denoted by angular brackets, e.g. $Q^m = \langle\widetilde{U}\rangle(x, r)$. The specific objective of the present work is to study the influence of $\Delta(\boldsymbol{x})$ on statistics of the resolved velocity and mixture fraction fields

Table 2. Grid resolutions for the jet nozzle and the pilot.

Grid	Cells in $\hat{x}$ for $\hat{x} < 0$	Cells in $\hat{r}$ for jet nozzle	Cells in $\hat{r}$ for pilot	Cells in jet nozzle wall	Cells in pilot wall
G1	3	10	15	2	2
G2	5	15	22	3	3
G3	8	20	30	3	4
G4	8	30	45	4	6
G5	9	40	50	5	7

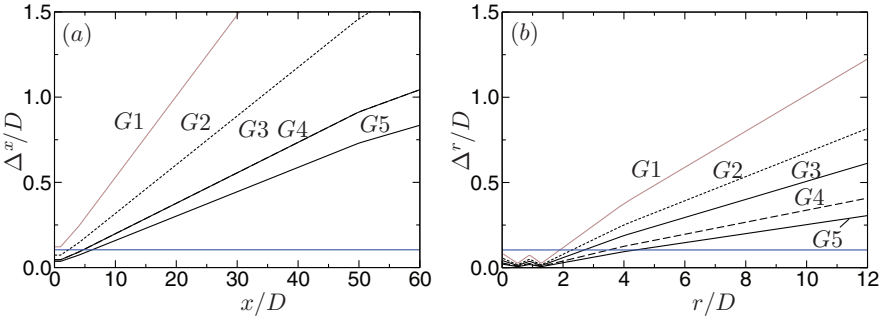

Figure 2. Grid resolutions for $G1$–$G5$ grids in the axial (a) and radial (b) directions compared with spatial resolution of the scalar measurements equal to $0.10416D$ [24], and shown by a horizontal line. Two minima in the radial resolutions correspond to grid clustering near the jet nozzle and pilot walls.

with respect to two different ways of treating the SGS variance V_ξ expressed by models I and II, respectively.

4. Results and discussion

4.1. *Resolved velocity field*

Axial profiles of the mean centreline streamwise velocity for models I and II on different grids are shown in Figures 3(a) and (b), respectively. The velocities shown in these figures are normalised by the jet bulk velocity. It is seen that both models exhibit convergence to almost the same asymptotic state starting with the $G3$ grid, while slightly overpredicting the mean velocity after axial location of $x/D = 20$. This is further evident from radial profiles of the mean and *rms* streamwise velocity shown in Figures 4 and 5 for axial locations of $x/D = 7.5$, 15, 30 and 45. For both variance models the mean and *rms* velocity fields demonstrate convergence at the same rate and to the same state, which is well described by the $G3$ grid solution. Overall, the mean and *rms* velocities for the converged state ($G3$–$G5$) are in good agreement with the experimental values, except a small overprediction of the mean streamwise velocity near the centreline at axial locations of $x/D = 30$ and 45.

The *rms* velocity fields from both models are characterised by the convergence 'from above', where the higher *rms* values are observed on the coarser grids. This is probably due to the fact that finer grids tend to resolve velocity gradients better, resulting in higher values of the resolved strain rate which diminish the *rms* velocity fluctuations because of the higher dissipation rate, and in spite of the lower values of the turbulent eddy viscosity.

The dependence of the resolved velocity statistics on Δ at particular axial and radial locations is shown in Figure 6. Here, the mean and *rms* of the streamwise velocity are plotted versus the grid spacing measure h ($\sim\Delta$). Since all grids are non-uniform, the grid spacing measure h is taken to be the inverse of the number of cells in the jet in the radial direction. The particular choice of these location points is related to the convergence of the mixture fraction variance and is discussed in the next section. Figure 6 demonstrates convincing convergence of the resolved velocity statistics for both variance models. Thus, density changes due to the SGS mixture fraction variance which happen to attain higher values for model II seem to have a marginal effect on the resolved *rms* velocity as it is almost identical for both models. Finally, we can conclude that as far as the statistics of the resolved velocity is concerned, both variance models produce equivalent results.

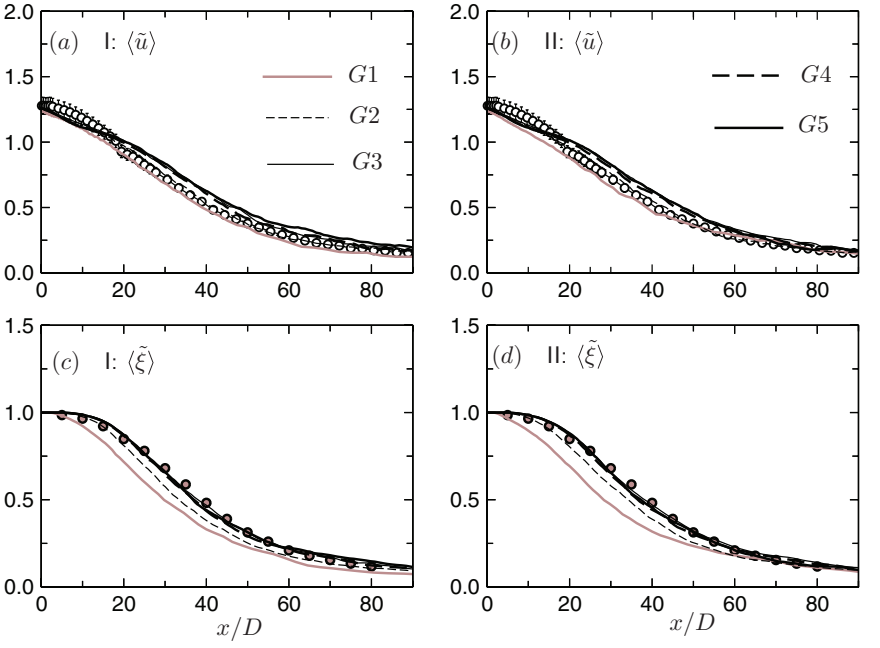

Figure 3. Axial profiles of the centreline mean streamwise velocity (a, b) and mean mixture fractions (c, d) for models I and II for different grids $G1$–$G5$ compared with the experimental data (circles) [24, 25]. The error bars on the experimental velocity profiles show the statistical uncertainties as reported in [25].

It is further remarked here that comparison with experimental data assists the present discussion only marginally. For example, it is interesting to note that the coarsest $G1$ grid provides the best approximation to the experimental values of the *rms* of the streamwise velocity at $x/D = 45$ as well as a reasonably good approximation to the experimental mean streamwise velocity on the centreline, which, nevertheless, does not make this LES solution satisfactory. It is also the case that experimental data contains some errors and uncertainty. But however imperfect, it is better to make comparison with experimental data than not to do so.

4.2. *Resolved mixture fraction field*

Figures 3(c) and (d) show axial profiles of the mean mixture fraction for models I and II, respectively. On the jet centreline, both models approximate the experimental data quite well showing convergence for the three finest grids. The results obtained are comparable to those of Ihme and Pitsch in their recent study [22] which employs the same code, a grid close to $G3$ but a different combustion model – the extended flamelet/progress variable model. It is interesting to note that a simple combustion model adopted here leads to the overprediction of the axial experimental values of the mean temperature field (not shown here and discussed in [15]) by about 100 K at downstream locations, which is similar to a trend reported by Ihme and Pitsch, and by other authors [30], and which can be linked to not accounting for the radiation effects in the flamelet models [38]. Radial profiles of the mean mixture fraction as well as the resolved variance $Q^W = \tilde{\xi}^2_{rms} = [\langle(\tilde{\xi})^2\rangle - \langle\tilde{\xi}\rangle^2]$, SGS

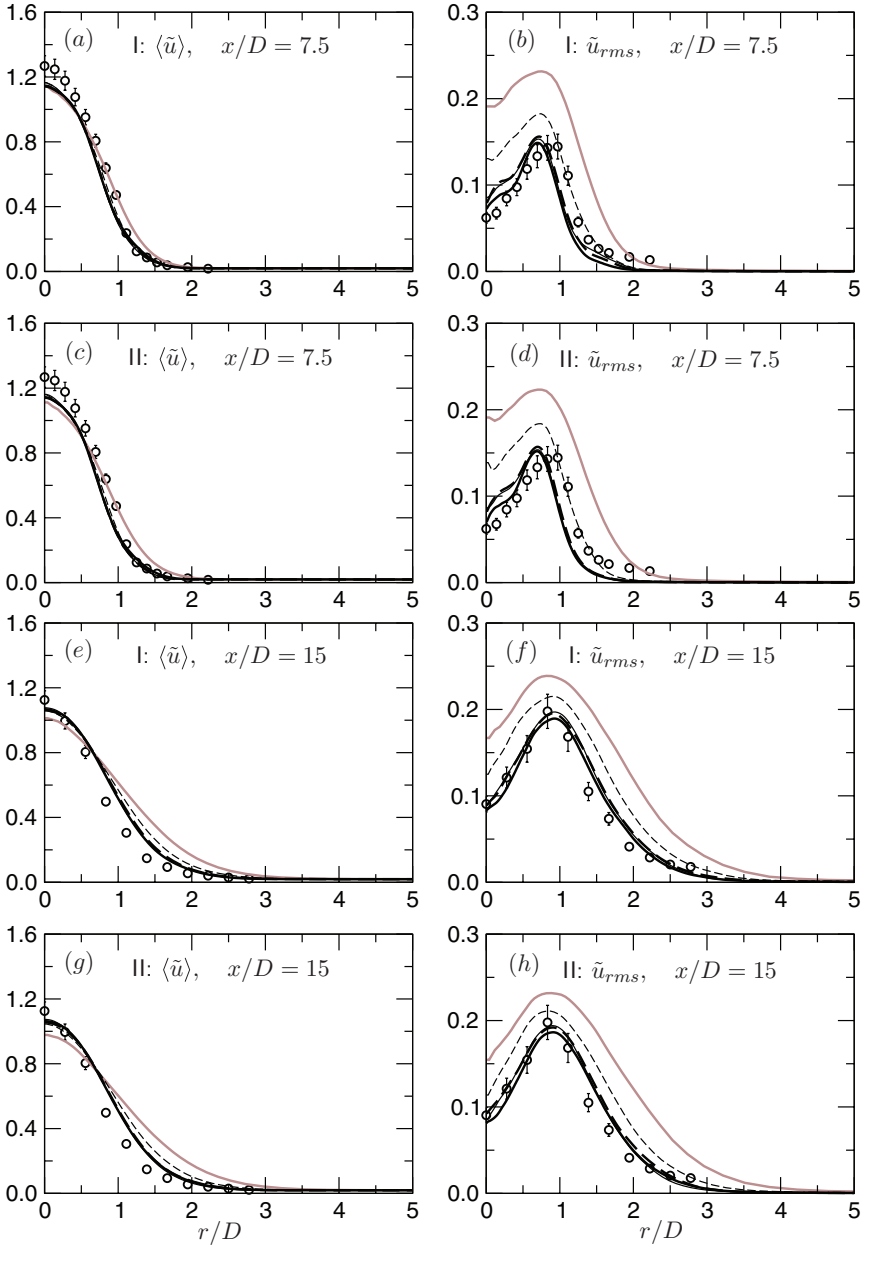

Figure 4. Radial profiles of mean and *rms* of streamwise velocity for models I (a, b, e, f) and II (c, d, g, h) at axial locations of $x/D = 7.5$ and 15 compared with the experimental data (circles). Results are obtained on grids: $G1$ – grey line, $G2$ – dashed thin line, $G3$ – solid thin line, $G4$ – dashed line and $G5$ – solid line. Note that the mean profiles on the $G3$–$G5$ grids become indistinguishably close. The error bars on the experimental profiles show the statistical uncertainties as reported in [25].

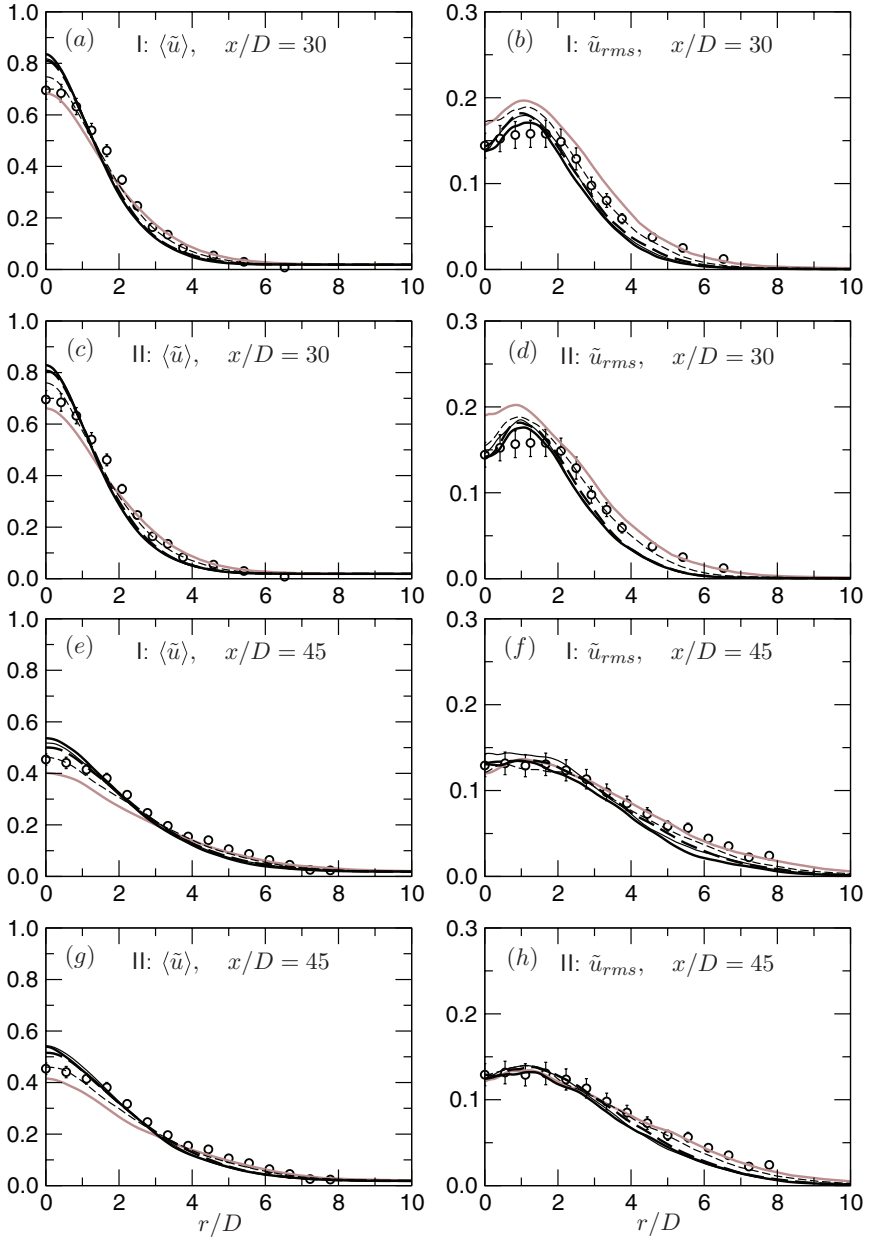

Figure 5. Radial profiles of mean and *rms* of streamwise velocity for models I (a, b, e, f) and II (c, d, g, h) at axial locations of $x/D = 30$ and 45 compared with the experimental data (circles). Results are obtained on grids: $G1$ – grey line, $G2$ – dashed thin line, $G3$ – solid thin line, $G4$ – dashed line and $G5$ – solid line. Note that the mean profiles on $G3$–$G5$ grids become indistinguishably close. The error bars on the experimental profiles show the statistical uncertainties as reported in [25].

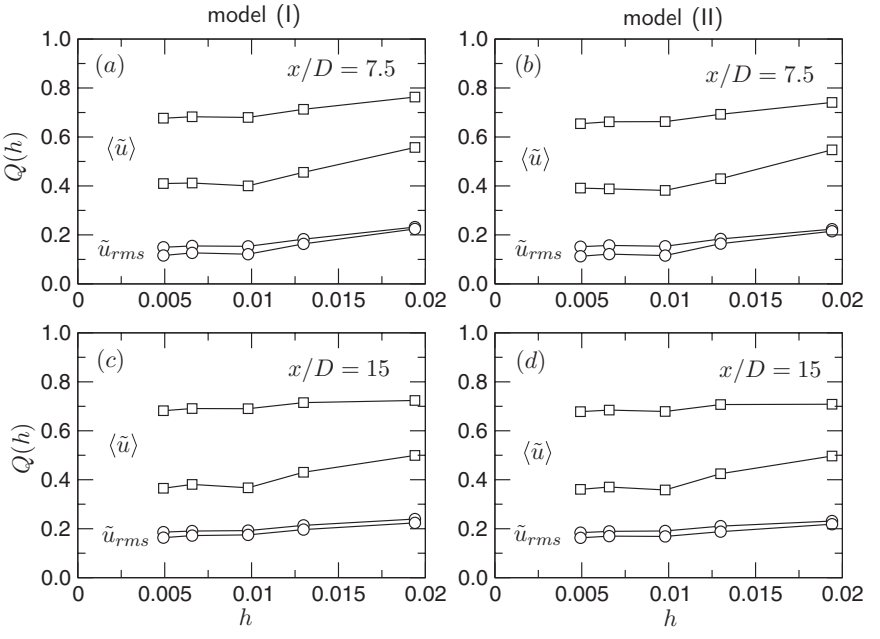

Figure 6. Convergence of the resolved velocity statistics $\langle\tilde{u}\rangle$ (squares) and $\tilde{u}_{rms}$ (circles) with grid spacing h ($\sim\Delta$) for model I (a, c) and model II (b, d) at axial locations of $x/D = 7.5$ and 15. Each statistics is shown at two radial locations: $r/D = 0.7$ (upper line) and $r/D = 0.9$ (lower line) for $x/D = 7.5$ and $r/D = 0.8$ (upper line) and $r/D = 1.2$ (lower line) for $x/D = 15$.

variance $Q^r = \langle V_\xi \rangle$ and total variance $Q^m = Q^W + Q^r$ of the mixture fraction are shown in Figures 7–10 at axial locations of $x/D = 7.5$, 15, 30 and 45. In these figures, top and bottom rows correspond to models I and II, respectively.

The mean mixture fraction fields from both models demonstrate convergence to the same solution on $G3$, $G4$ and $G5$ grids in most of the domain. In general, this convergent behaviour also characterises the resolved mixture fraction variances, but it is somewhat more complicated. It is seen from Figure 7 that in the near-field at $x/D = 7.5$ the resolved variances exhibit a visible sensitivity to the turbulent resolution scale Δ at the locations of their maxima ($r/D \sim 0.5$–0.75), i.e. in a mixing layer between cold jet fuel and hot pilot products. This can be related to a strong decrease of the turbulent subgrid diffusivity $\bar{\rho}\mathcal{D}_T$ in this region as grids are more and more refined, while the molecular diffusivity $\bar{\rho}\widetilde{\mathcal{D}}$ remains unchanged and smaller than its peak values because of temperature. Therefore, changes in turbulent subgrid diffusivity are contributing more to changes in the total diffusivity which results in less dissipation for finer grids and promotes higher values of the resolved mixture fraction variance. Further downstream at $x/D = 15$ and 30, the resolved mixture fraction variance shows less sensitivity to Δ and reaches an approximate convergent state on all $G3$–$G5$ grids (Figures 8 and 9). Here, the peak locations of the resolved variance are around $r/D = 1$, where the temperature is the highest and so is the molecular diffusivity, which dominates the subgrid diffusivity. At far field locations, for example at $x/D = 45$ (Figure 10), the convergence in variance is less convincing, especially for model II. The reason for this could be two-fold: first, the far field locations clearly require longer runs to accumulate an equivalent statistically representative ensemble (compared to near-field

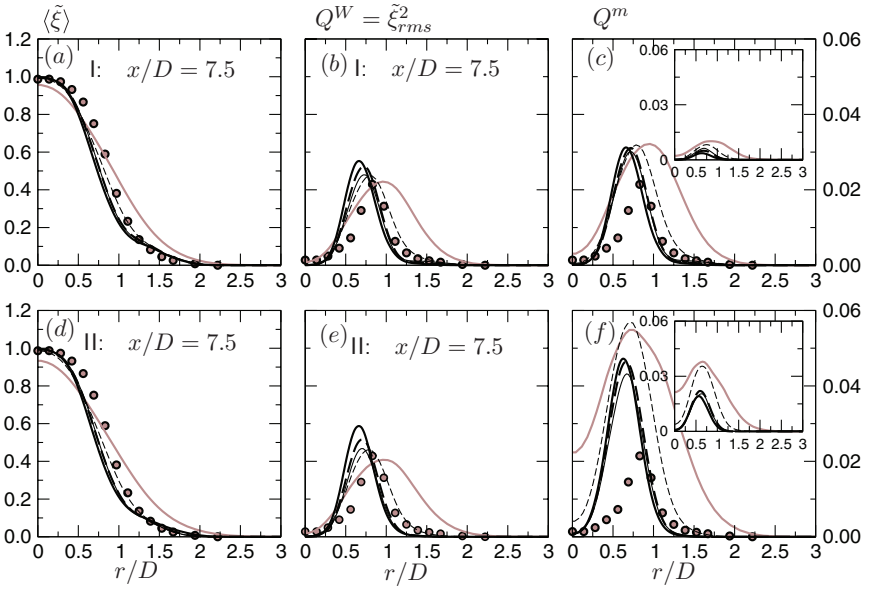

Figure 7. Radial profiles of mean (a, d), resolved variance – Q^W (b, e) and total variance (c, f) $Q^m = Q^W + Q^r$ of the mixture fraction for models I (top row) and II (bottom row) at an axial location of $x/D = 7.5$ for grids: $G1$ (grey), $G2$ (dashed), $G3$ (thin), $G4$ (bold dashed) and $G5$ (bold). Insets in (c, f) show residual variance profiles, $Q^r = \langle V_\xi \rangle$. Experimental data – circles [24].

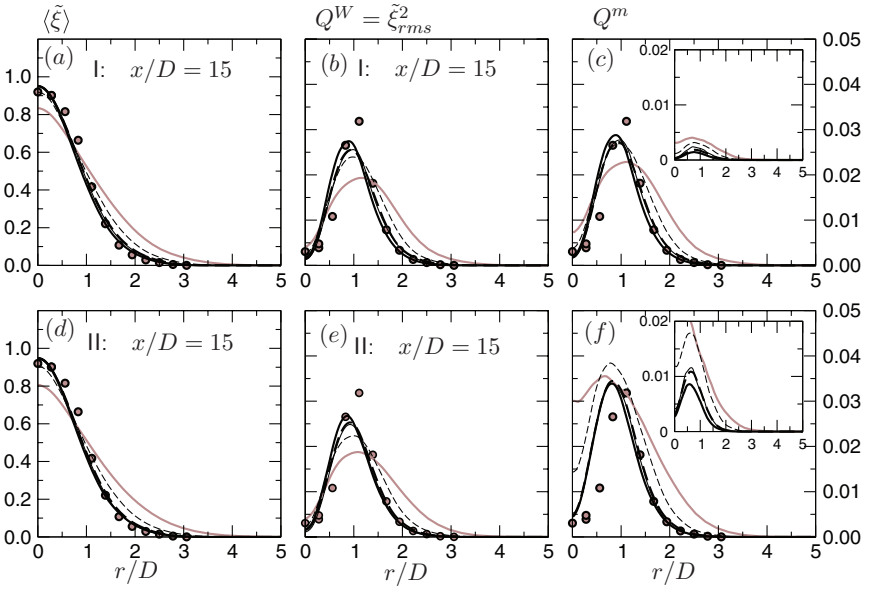

Figure 8. Radial profiles of mean (a, d), resolved variance – Q^W (b, e) and total variance (c, f) $Q^m = Q^W + Q^r$ of the mixture fraction for models I (top row) and II (bottom row) at an axial location of $x/D = 15$. Insets in (c, f) show residual variance profiles, $Q^r = \langle V_\xi \rangle$.

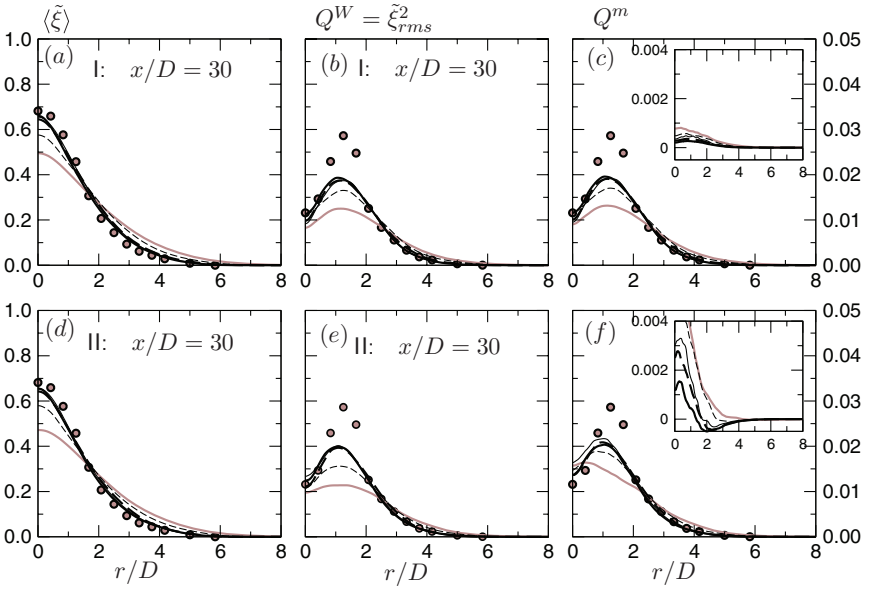

Figure 9. Radial profiles of mean (a, d), resolved variance – Q^W (b, e) and total variance (c, f) $Q^m = Q^W + Q^r$ of the mixture fraction for models I (top row) and II (bottom row) at an axial location of $x/D = 30$. Insets in (c, f) show residual variance profiles, $Q^r = \langle V_\xi \rangle$.

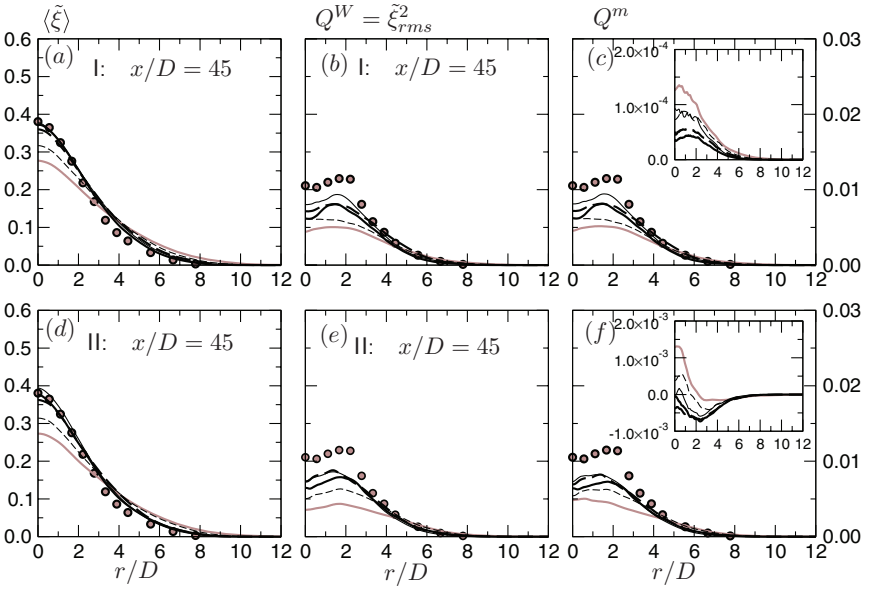

Figure 10. Radial profiles of mean (a, d), resolved variance – Q^W (b, e) and total variance (c, f) $Q^m = Q^W + Q^r$ of the mixture fraction for models I (top row) and II (bottom row) at an axial location of $x/D = 45$. Insets in (c, f) show residual variance profiles, $Q^r = \langle V_\xi \rangle$.

locations); second, the increase in cell size due to stretching in the axial direction may be excessive.

Comparing the resolved mixture fraction variance profiles of models I and II with the experimental data, it is seen that they overpredict the experimental values in the near field ($x/D = 7.5$), they are in general agreement with the experimental values at $x/D = 15$, and they start consistently underpredicting the experimental maximum values from $x/D = 30$. This suggests a non-constant value of the coefficient in a model for the SGS dissipation rate given by Equation (7). Model II is characterised by slightly higher levels of the resolved mixture fraction variance up to $x/D = 7.5$. These differences, however, become negligible as the jet develops further downstream. The major noticeable difference between the considered variance models comes from the mean values of the SGS mixture fraction variance as is evident from Figures 7–10. In the case of the mixture fraction square equation (model II) the SGS variance in the near-field (for $x/D < 15$) attains two to three times higher values compared to that obtained in model I. It is seen from Figure 7 that closer to the jet nozzle the SGS variance given by model II is even larger than the corresponding resolved variance on the first two grids while being comparable in magnitude for the $G3$–$G5$ grids. This leads to a gross overprediction of the total variance for axial location of 7.5 compared to the results of model I. The higher levels of the SGS variance obtained in model II can be attributed to negative values of the extra source term r_h, possibly, due to underprediction of the scalar gradient values as discussed earlier in Section 2.2. Further downstream (for $x/D \geq 15$), as the scalar gradient becomes weak, the SGS mixture fraction variance decreases rapidly and provides the smaller contribution to the total variance, but is still significant (about 30% on the $G5$ grid) in case of model II. Beyond an axial location of $x/D = 30$ the contribution of the SGS mixture variance is negligible.

An important difference between the two models is highlighted in Figures 9 and 10, which show that the mean SGS variance computed with model II develops negative values as the grid becomes more refined and one moves downstream. Thus, in this region model II loses the physical realisability property. In contrast, the SGS variance computed with model I monotonically decreases but always stays positive. One possible reason for that stems from the fact that the discrete $(\tilde{\xi})^2$ does not satisfy the corresponding discrete conservation equation (Equation 19). Qualitatively, when the turbulence resolution scale Δ decreases towards the DNS limit, S_ξ tends to s_ξ ($s_\xi \equiv (\tilde{\xi})^2$) while always satisfying its governing equation (Equation 9). This convergence is from above since one has $S_\xi \geq s_\xi$ because of $S_\xi = s_\xi + V_\xi$ and non-zero SGS variance V_ξ which is supposed to vanish in the DNS limit. On the other hand, since $(\tilde{\xi})^2$ in the discrete version of Equation (10) is directly obtained from the discrete mixture fraction field it does not satisfy Equation (13) for the square of the resolved mixture fraction at the discrete level. As a result, there is no reason to expect that both terms on the right-hand side of the discrete version of Equation (10), i.e. $V_\xi^{\mathrm{II}} = S_\xi - (\tilde{\xi})^2$, would experience convergence to their DNS values at the same rate as Δ goes towards the DNS limit. In particular, on the finer grids the first-order statistics of $(\tilde{\xi})^2$ can be found converged earlier than that of S_ξ. In other words, there exists some resolution scale Δ^* starting from which the mean values of $(\tilde{\xi})^2$ would exhibit a 'zero' convergence rate while the mean of S_ξ would continue to converge. Thus, it cannot be ruled out that for smaller values of the SGS variance the mean values of S_ξ catch up with those of $(\tilde{\xi})^2$ and even become smaller resulting in the appearance of negative regions of the mean SGS variance V_ξ^{II}.

This scenario seems to receive some confirmation from the inset to Figure 9(f), which shows a negative region in $\langle V_\xi^{\mathrm{II}} \rangle$ between radial locations of $r/D = 1.7$ and 4, approximately.

Simultaneously, Figures 9(*d*) and 9(*e*) show that both the mean mixture fraction $\langle\tilde{\xi}\rangle$ and the resolved mixture fraction variance $\tilde{\xi}^2_{rms}$ are fully converged there on the *G*3–*G*5 grids, hence the sum $\langle\tilde{\xi}^2\rangle = \langle\tilde{\xi}\rangle^2 + \tilde{\xi}^2_{rms}$ is converged also. Therefore, $\langle V^{\mathrm{II}}_{\xi}\rangle = \langle S_{\xi}\rangle - \langle\tilde{\xi}^2\rangle$ may become negative since the last term is nearly independent of Δ because of the convergence, while the first term continues to decrease because the DNS limit has not been reached yet. Note that non-decreasing of the first term would be equivalent to the existence of non-vanishing variance at the DNS limit, which is undesirable and leads to inconsistent formulation. To make the convergence rate of the mean $(\tilde{\xi})^2$ consistent with that of the mean S_{ξ} at the discrete level and towards the DNS limit, one needs to make $(\tilde{\xi})^2$ satisfy the governing equation for s_{ξ} at the discrete level, which is equivalent to employing model I with V^{I}_{ξ} defined by Equation (8). Finally, we would like to point out that while the results obtained clearly prove that model II is not realisable they are not sufficient to prove that model I is always realisable.

The dependence of the LES statistics on the turbulence resolution scale is further highlighted in Figures 11, 12 and 13. Here, the mean values of the mixture fraction are plotted versus the grid spacing measure h in Figure 11. The resolved, SGS and total variances of the mixture fraction are shown in Figures 12 and 13. These profiles correspond to two radial locations for each of the two axial locations considered ($x/D = 7.5$ and 15). The first radial location is taken to be around the maximum of the resolved variance, and the second location is shifted towards the lean side, i.e. $r/D = 0.7$, 0.9 and $r/D = 0.79$, 1.2 for $x/D = 7.5$ and 15, respectively. Figure 11 demonstrates convincing convergence of the mean mixture fraction $\langle\tilde{\xi}\rangle$ almost everywhere for both models on grids *G*3–*G*5, albeit

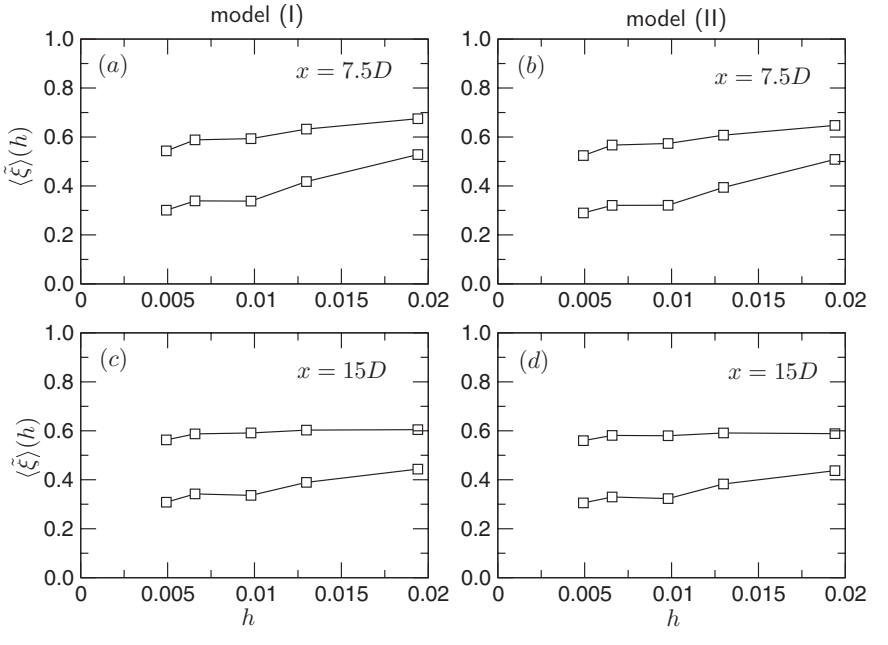

Figure 11. Convergence of the mean mixture fraction $\langle\tilde{\xi}\rangle$ with grid spacing h ($\sim\Delta$) for model I (a, c) and model II (b, d) at axial locations of $x/D = 7.5$ and 15. Each plot shows $\langle\tilde{\xi}\rangle(h)$ at two radial locations: $r/D = 0.7$ (upper line) and $r/D = 0.9$ (lower line) for $x/D = 7.5$ and $r/D = 0.8$ (upper line) and $r/D = 1.2$ (lower line) for $x/D = 15$.

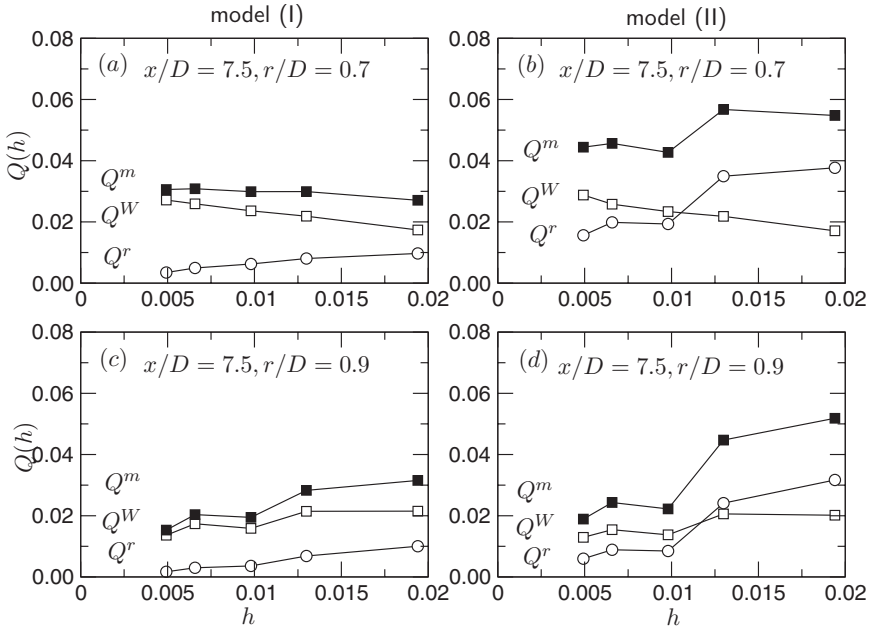

Figure 12. Convergence of the mixture fraction variances Q^W, Q^r and Q^m with grid spacing h ($\sim\Delta$) for model I (a, c) and model II (b, d) at two radial locations of $r/D = 0.7$ and 0.9 at $x/D = 7.5$.

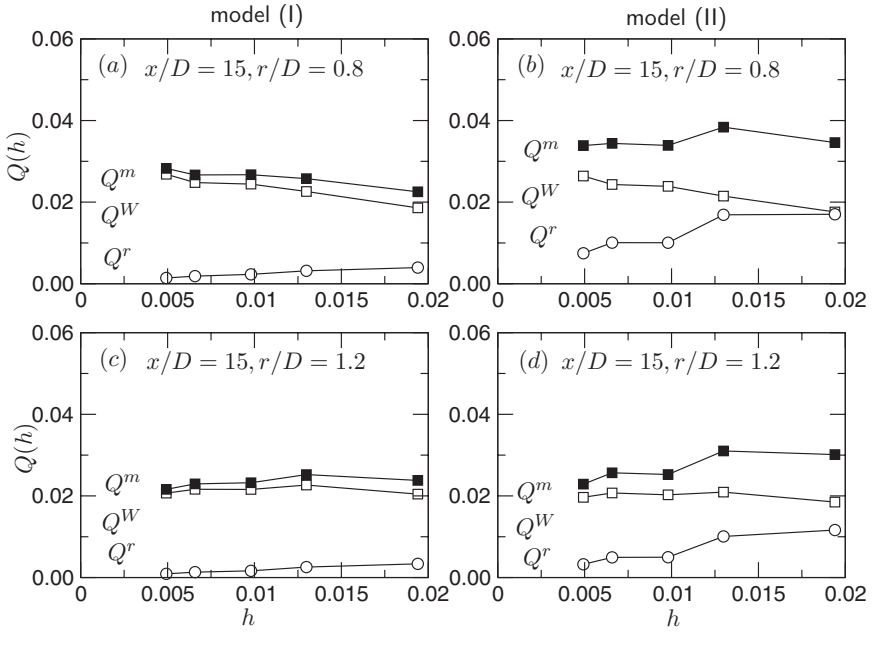

Figure 13. Convergence of the mixture fraction variances Q^W, Q^r and Q^m with grid spacing h ($\sim\Delta$) for model I (a, c) and model II (b, d) at two radial locations of $r/D = 0.8$ and 1.2 at $x/D = 15$.

with a slight decrease on grid $G5$. Figures 12 and 13 clearly reveal significant differences in the calculations of mixture fraction variance provided by the two models. For model I there is good convergence of the total modelled variance Q^m on grids $G3$–$G5$ (albeit with variation for grid $G5$ at $x = 7.5D$ and $r = 0.9D$); and the residual contribution Q^r is relatively small. For model II, the residual contribution is much larger; and it appears to be too large, in that Q^m generally decreases as the grid is refined. At the inner radial location, Q^m given by model II appears to converge for grids $G3$–$G5$, but to a larger value than given by model I. Note that Q^W given by model II agrees with the model I asymptote, and it is plausible that the higher values of Q^m for model II are due to spuriously large contributions from Q^r. Simulations on yet finer grids would be needed to confirm this hypothesis. It is also interesting to note that at the inner locations the total variance Q^m appears to be better converged on the three finer grids than the resolved variance Q^W for both models. Thus, the residual variance Q^r properly compensates for slow convergence of the resolved variance Q^W.

From calculations of the mixture fraction presented above, we conclude that model I is distinctly advantageous over model II. This is based on (i) the superior convergence properties of model I exhibited in Figures 12 and 13, and (ii) the fact that model I is realisable, whereas model II yields negative variances in some parts of the flow (insets in Figures 9 and 10). It should be appreciated that the difference between the two models is in their numerical implementations, and hence this conclusion pertains to the numerical schemes employed in the current LES code. However, as follows from the discussion in Section 2.2, this conclusion could be relevant for a rather wide class of numerical schemes for which the extra numerical source term r_h assumes non-negligible negative values.

5. Conclusions

LES of the piloted non-premixed Sandia flame D has been performed on a series of grids with progressively increasing resolution from 0.19 to 10.4 million cells, with the purpose of studying the sensitivity of LES statistics to the turbulence resolution scale Δ and to modelling the mixture fraction variance. A simple combustion model has been adopted to parametrise reacting density and temperature in terms of the mixture fraction and its subgrid variance, which utilises a quadratic B-spline approximation. Spline coefficients for quadratic analytic approximations of specific volume and temperature have been obtained based on a flamelet CHEMKIN simulation with a detailed chemistry mechanism. Simplicity and analytic representation eliminates the effect of the flamelet table interpolation errors on an LES solution and its statistics.

Two approaches to modelling the SGS variance were analysed. The first one (model I) adopts a transport equation for the SGS variance, while in the second one (model II), a transport equation for the square of the mixture fraction is used. These models are equivalent in the continuous sense with the only difference arising from different numerical approximation errors. The observed differences between the two models are attributed to numerical errors arising from not enforcing the conservation property in model II for the square of the mixture fraction at the discrete level. It manifests itself as the appearance of an extra numerical source term when the discrete governing equations for both models are written in the equivalent form. However, due to the relative insensitivity of the considered flame configuration to the incurred errors in the SGS variance, the obtained statistics of the resolved LES fields are quite comparable and reproduce the essential features of Sandia flame D well. It is anticipated that in more challenging flame regimes involving

auto-ignition, flame stabilisation and dilution by burnt products the models would exhibit appreciable differences in LES solutions.

The results obtained demonstrate that the LES statistics exhibit clearly identifiable convergence regions with respect to Δ. However, these regions are different and depend on the type of LES statistics (mean or variance) and flow variables (velocity or mixture fraction) considered. In the jet near-field ($x/D \geq 15$) the mean LES velocity exhibits convergence at the larger turbulence resolution scale than the corresponding variance field does. Overall, the LES velocity statistics are shown to be convergent throughout the flow domain on the three finest grids for both models. Both statistics (mean and variance) of the resolved mixture fraction demonstrate consistent convergence on the three finest grids, the only exceptions being small regions of high scalar gradients where the resolved mixture fraction variance is found to converge more slowly.

To analyse the total LES variance the residual variance contribution has been estimated as the mean SGS variance based on models I and II. The results obtained show that the total LES variance exhibits better convergence properties than the resolved variance irrespective of the model chosen for the residual variance, emphasising the importance of accounting for the residual contribution in LES statistics. Thus, the total LES statistics Q^m can be used for an approximate identification of convergent/non-convergent regions of flow which is important in developing an adaptive LES implementation [7].

While in model I the mean SGS variance exhibits physical realisability everywhere ($\langle V_\xi^{\mathrm{I}} \rangle \geq 0$), its square mixture fraction counterpart (model II) is characterised by the existence of negative regions ($\langle V_\xi^{\mathrm{II}} \rangle \leq 0$) in the far field of the jet ($x/D \geq 30$) on the finer grids. Model II always predicts higher values of the SGS variance. Moreover, given statistical errors, it is plausible that the model I total variances on grids $G3$–$G5$ are within a small neighbourhood (say 5%) of the asymptotic value. Overall, due to (i) convincingly better convergence properties with respect to the turbulence resolution scale Δ, (ii) observed physical realisability everywhere, and (iii) the formulation which facilitates conservation at the discrete level, model I provides a clear advantage over model II pertaining to the conducted LES of Sandia flame D.

Furthermore, more generally, the approach adopted in this work also provides a framework for examining the consistency of the LES statistics at the DNS limit by drawing a comparison between the total and resolved LES statistics estimated at $\Delta \to 0$. An LES model is deemed to be consistent at the DNS limit if both statistics are equal.

Acknowledegments

This work was supported by the Air Force Office of Scientific Research (AFOSR) under Grant No. FA-9550-09-1-0047 and by Grant No. FA-9550-09-1-0611 funded by AFOSR and NASA ARMD, technical monitors Julian Tishkoff (AFOSR), Aaron Auslender and Rick Gaffney (NASA). This research was also supported in part by the National Science Foundation through TeraGrid resources provided by the Texas Advanced Computing Center under Grant No. TG-CTS090020.

References

[1] T. Poinsot and D. Veynante, *Theoretical and Numerical Combustion*, R.T. Edwards, Philadelphia, PA, 2005.

[2] H. Pitsch, *Large-eddy simulation of turbulent combustion*, Annu. Rev. Fluid Mech. 38 (2006), pp. 453–482.

[3] W.W. Kim, S. Menon, and H.C. Mongia, *Large-eddy simulation of a gas turbine combustor flow*, Combust. Sci. Technol. 143 (1999), pp. 25–62.

[4] F. di Mare, W.P. Jones, and K.R. Menzies, *Large eddy simulation of a model gas turbine combustor*, Combust. Flame 137 (2004), pp. 278–294.
[5] K. Mahesh, G. Constantinescu, S. Apte, G. Iaccarion, F. Ham, and P. Moin, *Large-eddy simulation of reacting turbulent flows in complex geometries*, J. Appl. Mech. 73 (2006), pp. 374–381.
[6] G. Boudier, L.Y.M. Gicquel, and T.J. Poinsot, *Effects of mesh resolution on large eddy simulation of reacting flows in complex geometry combustors*, Combust. Flame 155 (2008), pp. 196–214.
[7] S.B. Pope, *Ten questions concerning the large-eddy simulations of turbulent flows*, New J. Phys. 6 (2004), p. 35.
[8] T. Hughes, L. Mazzei, and K. Jansen, *The large eddy simulation and variational multiscale method*, Comput. Visualiz. Sci. 3 (2000), pp. 47–59.
[9] J.L. Guermond, J.T. Oden, and S. Prudhomme, *Mathematical perspective on large eddy simulation models for turbulent flows*, J. Math. Fluid Mech. 6 (2004), pp. 195–248.
[10] N. Peters, *Laminar diffusion flamelet models in non-premixed turbulent combustion*, Prog. Energy Combust. Sci. 10 (1984), pp. 319–339.
[11] C.D. Pierce and P. Moin, *Progress-variable approach for large-eddy simulations of non-premixed turbulent combustion*, J. Fluid Mech. 504 (2004), pp. 73–97.
[12] S.B. Pope, *PDF methods for turbulent reacting flows*, Prog. Energy Combust. Sci. 11 (1985), pp. 119–192.
[13] A.W. Cook and J.J. Riley, *A subgrid model for equilibrium chemistry in turbulent flows*, Phys. Fluids 6 (1994), pp. 2868–2870.
[14] J. Jiménez, A. Liñán, M.M. Rogers, and F.J. Higuera, *A priori testing of subgrid models for chemically reacting non-premixed turbulent shear flows*, J. Fluid Mech. 349 (1997), pp. 149–171.
[15] K.A. Kemenov and S.B. Pope, *Molecular diffusion effects in LES of a piloted methane–air flame*, Combust. Flame 158 (2011), pp. 240–254.
[16] C.D. Pierce and P. Moin, *A dynamic model for subgrid-scale variance and dissipation rate of a conserved scalar*, Phys. Fluids 10 (1998), pp. 3041–3044.
[17] C. Jiménez, F. Ducros, B. Cuenot, and B. Bédat, *Subgrid scale variance and dissipation of a scalar field in large eddy simulations*, Phys. Fluids 13 (2001), pp. 1748–1754.
[18] C. Pera, J. Réveillon, L. Vervisch, and P. Domingo, *Modeling subgrid scale mixture fraction variance in LES of evaporating spray*, Combust. Flame 146 (2006), pp. 635–648.
[19] G. Balarac, H. Pitsch, and V. Raman, *Development of a dynamic model for the subfilter scalar variance using the concept of optimal estimators*, Phys. Fluids 20 (2008), p. 035114.
[20] C.M. Kaul, V. Raman, G. Balarac, and H. Pitsch, *Numerical errors in the computation of subfilter scalar variance in large eddy simulations*, Phys. Fluids 21 (2009), p. 055102.
[21] V. Raman, H. Pitsch, and R.O. Fox, *Hybrid large-eddy simulation/Lagrangian filtered-density-function for simulating of turbulent combustion*, Combust. Flame 143 (2005), pp. 56–78.
[22] M. Ihme and H. Pitsch, *Prediction of extinction and reignition in nonpremixed turbulent flames using a flamelet/progress variable model – 2. Application in LES of Sandia flames D and E*, Combust. Flame 155 (2008), pp. 90–107.
[23] A. Triantafyllidis, E. Mastorakos, and R.L.G.M. Eggels, *Large eddy simulations of forced ignition of a non-premixed bluff-body methane flame with conditional moment closure*, Combust. Flame 156 (2009), pp. 2328–2345.
[24] R.S. Barlow and J.H. Frank, *Effects of turbulence on species mass fractions in methane/air jet flames*, Proc. Combust. Inst. 27 (1998), pp. 1087–1095.
[25] C. Schneider, A. Dreizler, J. Janicka, and E.P. Hassel, *Flow field measurements of stable and locally extinguishing hydrocarbon-fueled jet flames*, Combust. Flame 135 (2003), pp. 185–190.
[26] H. Pitsch and H. Steiner, *Large-eddy simulation of a turbulent piloted methane/air diffusion flame (Sandia flame D)*, Phys. Fluids 12 (2000), pp. 2541–2554.
[27] A. Kempf, F. Flemming, and J. Janicka, *Investigation of lengthscales, scalar dissipation, and flame orientation in a piloted diffusion flame by LES*, Proc. Combust. Inst. 30 (2005), pp. 557–565.
[28] M.R.H. Sheikhi, T.G. Drozda, P. Givi, F.A. Jaberi, and S.B. Pope, *Large eddy simulation of a turbulent nonpremixed piloted methane jet flame (Sandia Flame D)*, Proc. Combust. Inst. 30 (2005), pp. 549–556.
[29] V. Raman and H. Pitsch, *A consistent LES/filtered-density function formulation for the simulation of turbulent flames with detailed chemistry*, Proc. Combust. Inst. 31 (2007), pp. 1711–1719.

[30] A.W. Vreman, B.A. Albrecht, J.A. van Oijen, L.P.H. de Goey, and R.J.M. Bastiaans, *Premixed and nonpremixed generated manifolds in large-eddy simulation of Sandia flame D and F*, Combust. Flame 153 (2008), pp. 394–416.
[31] D.J. Clayton and W.P. Jones, *Large eddy simulation of methane–air diffusion flame*, Flow Turbul. Combust. 81 (2008), pp. 497–521.
[32] R. Cabra, J.Y. Chen, R.W. Dibble, A.N. Karpetis, and R.S. Barlow, *Lifted methane–air flames in a vitiated coflow*, Combust. Flame 143 (2005), pp. 491–506.
[33] P. Domingo, L. Vervisch, and D. Veynante, *Large eddy simulation of a lifted jet flame in a vitiated coflow*, Combust. Flame 152 (2008), pp. 415–432.
[34] R.L. Gordon, A.R. Masri, S.B. Pope, and G.M. Goldin, *Transport budgets in turbulent lifted flames of methane autoigniting in a vitiated co-flow*, Combust. Flame 151 (2007), pp. 495–511.
[35] M. Germano, U. Piomelli, P. Moin, and W.H. Cabot, *A dynamic subgrid-scale eddy viscosity model*, Phys. Fluids A 3 (1991), pp. 1760–1765.
[36] D.K. Lilly, *A proposed modification of the Germano subgrid-scale closure method*, Phys. Fluids A 4 (1992), pp. 633–635.
[37] B.P. Leonard, *A stable and accurate convective modeling procedure based on quadratic upstream interpolation*, Computer Meth. Appl. Mech. Engng 19 (1979), pp. 59–98.
[38] M. Ihme and H. Pitsch, *Modeling of radiation and nitric oxide formation in turbulent non-premixed flames using a flamelet/progress variable formulation*, Phys. Fluids 20 (2008), p. 055110.